



## Coupling effects of multiple strengthening mechanisms in spheroidal microstructure eutectic high-entropy alloys

Jinliang Du<sup>a</sup>, Weijie Li<sup>b</sup>, Zhixin Huang<sup>a</sup>, Hangqi Feng<sup>a</sup>, Ying Li<sup>c,d,\*</sup>

<sup>a</sup> School of Naval Architecture, Ocean and Energy Power Engineering, Wuhan University of Technology, Wuhan, 430063, PR China

<sup>b</sup> School of Civil Engineering, Beijing Jiaotong University, Beijing, 100044, PR China

<sup>c</sup> State Key Laboratory of Explosion Science and Technology, Beijing Institute of Technology, Beijing, 100081, PR China

<sup>d</sup> Beijing Key Laboratory of Lightweight Multi-functional Composite Materials and Structures, Beijing Institute of Technology, Beijing, 100081, PR China



### ARTICLE INFO

#### Keywords:

Metallic material  
Microstructure  
Warm rolling  
Short-time annealing  
Yield strength

### ABSTRACT

The yield strength of metallic materials is commonly estimated using linear superposition methods, but this method has limited adaptability to new materials. The mapping relationship between input and output in machine learning methods is difficult to quantify. This study employs a rapid screening method to identify the key strengthening mechanisms that influence the yield strength of typical homogeneous and heterogeneous metallic materials. A non-linear physical neural information network model is developed to describe the yield strength of heterogeneous structures, capturing the main parameters contributing to yield strength from selected physical quantity data. By considering the non-linear strengthening mechanisms arising from interactions among multiple strengthening mechanisms in heterogeneous metal structures, the microstructure and mechanical properties of eutectic high-entropy alloys are optimized through warm rolling and short-time annealing. By inducing microstructural spheroidization and introducing nanoscale precipitates, significant coupling effects of multiple strengthening mechanisms are achieved for eutectic high-entropy alloys. As a result, the yield strength increases by approximately 2.5 times, while plasticity remains nearly unchanged. Transmission electron microscopy, scanning electron microscopy, and electron backscatter diffraction observations provide evidence for the sources of these coupling effects. This study offers guidance for accelerating material design and exploring the physical relationship between microstructure and mechanical properties.

### 1. Introduction

Metallic materials are the most widely used structural materials, and the improvement of their yield strength (YS) holds significant scientific and engineering importance [1–4]. Clarifying the inherent factors and physical mechanisms that influence YS, and achieving precise calculation and prediction of YS, have long been core scientific questions and major challenges in the field of materials mechanics. For a long time, it has been believed that the YS of metallic materials is influenced by strength and strengthening mechanisms [5–8]. For instance, large-sized homogeneous microstructure materials are primarily strengthened by grain boundaries, and the relationship between grain size and YS can be demonstrated by the Hall-Petch relationship [9–12], where it is assumed that the yield stress increases as the grain size decreases. Eric Hall and Norman Petch [13,14] suggested that the yield stress increases with decreasing grain size. Although grain refinement can significantly

improve the YS of the material, it is at the expense of plasticity [15–17]. In order to reconcile strength and plasticity, various methods such as dislocation engineering [18,19], twinning engineering [20,21], biomimetic engineering [22,23], lamellar microstructures [24–26], metastable microstructures [27,28], nano-biphasic/multiphasic microstructures [29–31], and heterogeneous microstructures [32–34] have been developed. Fig. 1 illustrates the development trend of microstructure design and development in composite metallic materials, such as ref. [35]. Despite the diversity in microstructure development, the description of YS has long been achieved through linear superposition rules (simple linear addition of multiple strengthening mechanisms, denoted as L-RR) [35,36]. Although L-RR partially complies with the basic mechanical laws governing YS, it often leads to different degrees of overestimation or underestimation for novel microstructured composite metallic materials, deviating from the need for rapid calculation of YS (Fig. 1). Elucidating the relationships between multiple

\* Corresponding author. State Key Laboratory of Explosion Science and Technology, Beijing Institute of Technology, Beijing, 100081, PR China.

E-mail address: [bitliying@bit.edu.cn](mailto:bitliying@bit.edu.cn) (Y. Li).

strengthening mechanisms in composite microstructures and YS poses certain challenges.

In recent years, there have been many studies exploring the relationship between key features of new structures and YS based on phenomenological theory. In the concept of heterostructure (HS) design, the strengthening mechanism of heterostructure materials (HSMs) is quantified using an updated linear strengthening rule considering the strain incompatibility of multiscale grain boundaries [32,33,37]. Ji et al. [38,39] established the softening model of grain size on YS using the molecular dynamics method. Combining dislocation stacking and slip theory, Liebig et al. (2018) provided new insights into the yield process of micropillars [40]. Considering the competitive strengthening between dislocation slip and twins, Woo et al. [41,42] optimized the linear strengthening rule for metastable structural materials. Dong and Li [43,44] respectively used surface strengthening and chemical strengthening to increase the yield strength of the material. In the development of new microstructures, a variety of new strengthening mechanisms have been found, including precursor strengthening [45], interfacial strengthening [46], shape memory alloy strengthening [47], etc., in addition to the above. The above research deepens the understanding of the yielding phenomenon in polycrystalline metals, but there is still a lack of methods to quantitatively establish the rules of strengthening mechanisms. Establishing a physical relationship that describes the yield strength of typical heterogeneous structured metallic materials holds significant importance for material design theory and engineering practice.

Heterogeneous structure design, as an emerging method, has attracted great attention to achieve superior strength-ductility synergy that cannot be achieved by traditional homogeneous materials. In the deformation process of heterogeneous structure materials [48], geometrically necessary dislocations (GNDs) accumulate due to mutual constraints between hard/soft domains. The accumulation of GNDs at domain boundaries leads to the coupling of heterogeneous deformation-induced (HDI) strengthening and multiple strengthening mechanisms while maintaining ductility. The HDI and cooperative hardening effects of heterogeneous structure result in better mechanical properties than predictions using “mixture rules” or “L-RR”. How to fully exploit this cooperative strengthening effect through the optimization of structural parameters has garnered attention.

Despite the extraordinary performance of heterogeneous structures, controlling their heterogeneity remains a challenging task. To achieve a robust cooperative strengthening effect, heterogeneity should be adjusted by controlling appropriate sizes, geometric shapes, and distributions. Various heterogeneous structures have been developed so far, including gradient structures, multiphase structures, lamellar structures,

bimodal structures, and biomimetic structures. However, the lack of a quantification method for the coupling effect of multiple strengthening mechanisms in heterogeneous alloys necessitates that structural design go through the tedious process of traditional routes from casting to annealing.

The data-driven method has excellent nonlinear fitting ability and has advantages in new material discovery [49,50]. The physical neural information model (PNIM) refers to the combination of prior knowledge of physics and data-driven machine learning models. This has become an effective approach to alleviate the shortage of training data, improve model generalization ability, and ensure the physical reasonableness of the results. Recent work in PNIM can be summarized in the following three points: (1) the integration of PNIM development with motivation and physics problems, (2) the physical knowledge of the input and output of PNIM, and (3) the physical phenomena and implications during the data transmission process in PNIM. The PNIM helps to reveal the complex physical mechanism between input and output by selecting key subsets of various strengthening mechanisms that affect YS [51]. It is worth noting that although PNIM can better fit YS based on structural parameters, the obtained network structure is often similar to a “black box”, and its complex mapping relationship is difficult to express and apply intuitively [52].

Based on the aforementioned background, this work proposes a data-driven approach to investigate the physical nature of the coupling effects of various strengthening mechanisms on yield strength (YS) and establishes an explicit expression for YS in heterogeneous structured high-entropy alloys (HEAs). The design features of lamellar eutectic high-entropy alloys (EHEAs) are explored, and a refined structural design method combining FCC, BCC, and nano-precipitates is proposed. Quantitative calculations are performed to assess the impact of different strengthening mechanisms and their nonlinear coupling effects on the YS of polycrystalline metals, providing new ideas and methods for the design and development of metallic materials.

## 2. Methods

### 2.1. Statistical assumptions

In the case of excessively high or low temperatures or strain fields, as mentioned above, the linear hardening rule for yield strength is an empirical formula used to describe the deformation behavior of materials. There may be some errors in the calculation process, which mainly come from the following aspects:

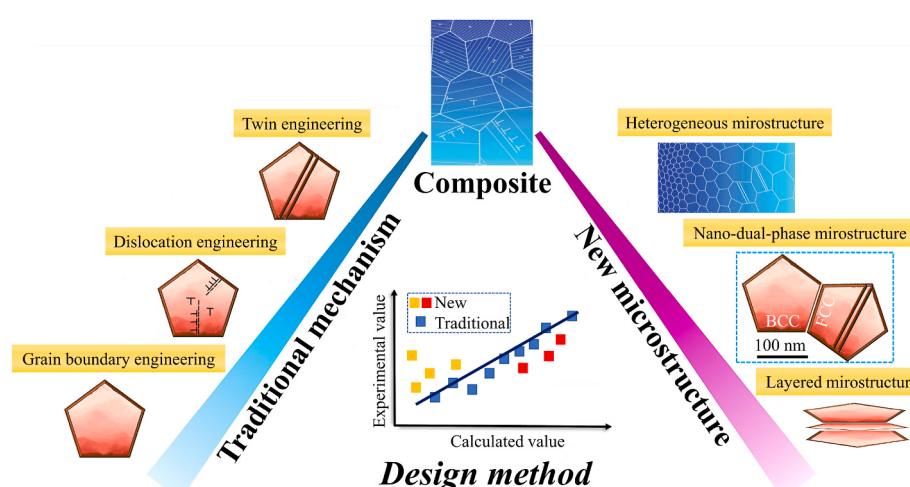


**Fig. 1.** The combination of traditional reinforcement mechanisms and new microstructural materials causes YS to deviate from L-RR.

- a. Experimental data errors: The calculation of the linear hardening rule typically relies on experimental data, including the stress-strain curve of the material and statistical data on the strengthening mechanisms. Measurement errors in experimental data directly affect the accuracy of the calculation results.
- b. Errors in basic calculation theory: The linear hardening rule is based on certain statistical assumptions, such as isotropic strain in single crystals or polycrystals, and elastic isotropy. However, these assumptions are not always strictly valid in practical materials, so there may be errors in the calculation results.
- c. Material non-uniformity: The microstructure and organization of materials determine their macroscopic properties and material non-uniformity can lead to variations in yield strength. The linear hardening rule does not consider material non-uniformity, so there may be deviations between the calculated results and the actual situation in some special cases.
- d. Effects of temperature and strain rate: The linear hardening rule is typically applicable to room temperature and low strain rate conditions. When the temperature rises or the strain rate increases, the deformation behavior of the material may change, leading to increased errors in the calculation results.

To obtain more accurate results, it is necessary to consider these influencing factors and make appropriate corrections in the calculation process. In terms of the reliability of experimental data, it is generally determined after the completion of the experiments and has a relatively minor impact on the core content of this work. Therefore, we assume that the process of obtaining and statistically analyzing experimental data is ideal. It has been confirmed that certain theories for plastic deformation in crystal structures can accurately guide the calculation of a specific strengthening mechanism, with negligible error. Under the effects of temperature and strain rate, the mechanical behavior of materials often exhibits anomalous phenomena.

The above-mentioned assumptions play an important role in the design of high-entropy alloy for enhancing strength and toughness, as well as in revealing the mechanism of non-linear strengthening. High-entropy alloys have complex microstructures and multi-element compositions, and their strong and tough design requires consideration of more complex factors, such as the interaction between elements and the

stability of crystal structures. For this special material, the assumption of linear hardening rule may have limitations in describing its deformation behavior, because the complexity of the material itself may lead to the emergence of non-linear strengthening mechanism. Therefore, it is necessary to further study and reveal the non-linear strengthening mechanism in high-entropy alloys, in order to more accurately evaluate their strength and toughness, and provide a more reliable basis for material design and engineering applications.

## 2.2. Multi-strengthening mechanism material design

We prepared eutectic high-entropy alloys with the composition AlCoCrFeNi<sub>2.1</sub> using a vacuum melting furnace (Fig. 2). After warm rolling at 600 °C, 700 °C, and 800 °C, short-time annealing is carried out in a vacuum heat treatment furnace. The holding temperature is 800 °C, and the holding time is 1 h. Using QUANTA FEG450-SEM to observe its microstructure, it was found that the composite structure of BCC, FCC, and nano-precipitated phase provided a complex strengthening mechanism, which was the reason for its high strength and high plasticity. The eutectic high-entropy alloy samples were cut and polished to obtain thin sheets with a thickness range of 50 μm. The thin sheets were then prepared using an electropolishing method with a solution composed of 10% volume fraction of high-concentration perchloric acid and 90% ethanol. We analyzed the microstructural features of the matrix and interface with the equipment JEM-2100F-TEM, verified the generalization performance of the new relationship, and revealed the fundamental physical meaning of the new formula. The ordinary and annealed eutectic high-entropy alloys were processed into dog-bone samples with a gauge length of 18 mm, a width of 2.5 mm, and a thickness of 1.5 mm. The quasi-static tensile test was carried out on an Instron 5565S testing machine with a strain rate of  $5 \times 10^{-4} \text{ s}^{-1}$ . To avoid the randomness of the experiment, each tensile test was repeated three times.

## 2.3. Feature recursive elimination

Recursive feature elimination based on the random forest model is a method used for feature selection. It constructs the random forest model in a recursive manner and performs feature ranking and selection by evaluating the importance of features. In this work, the Random Forest

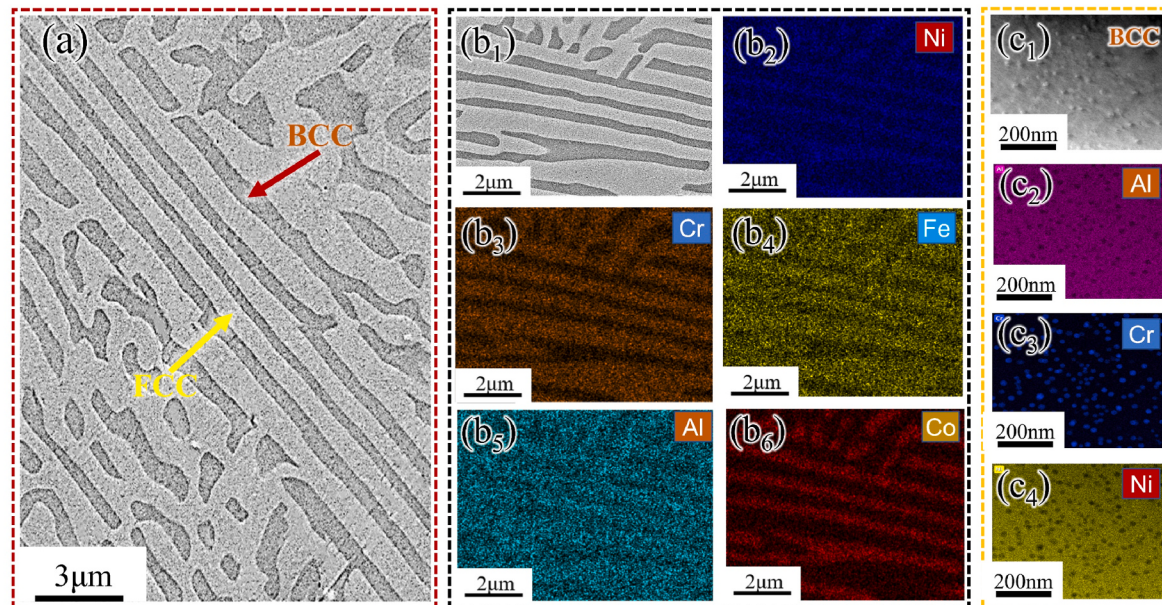


**Fig. 2.** Microstructure of initial AlCoCrFeNi<sub>2.1</sub> eutectic high-entropy alloy. (a) BCC and FCC present irregular and heterogeneous features. (b) energy spectrum analysis of the composition distribution of BCC and FCC, BCC is dominated by Co and Ni, FCC Mainly Al, Fe, Cr. (c) TEM found a large number of nano-scale precipitates dispersedly distributed on the BCC matrix, mainly Cr.

regressor is used as the basic model for iterative selection and importance ranking of 25 feature sets. The feature importance extracted by this method is typically achieved by taking the average of the predictions from each decision tree. By sorting the importance of each feature in the model, the lowest-ranked feature is removed from the current feature set in each iteration, with a step size of 1. The process continues until only 4 features remain, and the final feature set is returned. By comparing the results of the selection, it intuitively displays the features that have the most contribution to predicting the target variable.

#### 2.4. Pearson coefficient method for initial screening of key features

The Pearson correlation coefficient method is used to measure the correlation of metal material parameters, and the correlation coefficient is expressed by  $r$ . The closer the correlation coefficient  $r$  is to 1 or -1, the stronger the correlation is, and the closer the correlation coefficient is to 0, the correlation is the weaker. The Pearson correlation coefficient is simply the covariance of the two variables divided by the product of the standard deviations of the two variables:

$$r = \frac{\sum (X - \bar{X})(Y - \bar{Y})}{\left( \sqrt{\sum_{i=1}^n (X_i - \bar{X})^2} \right) \left( \sqrt{\sum_{i=1}^n (Y_i - \bar{Y})^2} \right)} \quad (10)$$

where  $X$  and  $Y$  represent two strengthening mechanisms. In order to better measure the degree of correlation between two random variables,

the Pearson correlation coefficient is divided by the standard deviation of the two random variables on the basis of the covariance, eliminating the influence of dimension.

### 3. Result and discussion

#### 3.1. Screening of physical quantities

The route of this research is shown in Fig. 3(a). From the relevant research literature, it is found that with the diversification of new structures and new processes, the number of discovered strengthening mechanisms for polycrystalline metal materials has reached 25, such as supplementary materials Table 1 shows. Among them, there are theoretical intersections between some strengthening mechanisms. We selected the strengthening mechanism of three typical materials with nano/ultrafine homogeneous structure (NG/UFG), coarse grain homogeneous structure (CG), and heterostructure (HS) as the data set for constructing machine learning, each The structure collects 100 sets of data, a total of 300 sets of data (set the ratio of the training set to test set to 8:2) [33,33,34]. The data set contains strengthening mechanisms of common structural materials: Ti alloys, Fe-based alloys, Al alloys, Mg alloys, high-entropy alloys, medium-entropy alloys, etc. Using the Pearson method [53] and the random forest recursive feature elimination method [54], the key feature subsets that affect the polycrystalline metal YS are extracted and determined. Based on the screened key physical quantities, an error backpropagation physical neural information network model (BPNN) is established. Using the excellent nonlinear

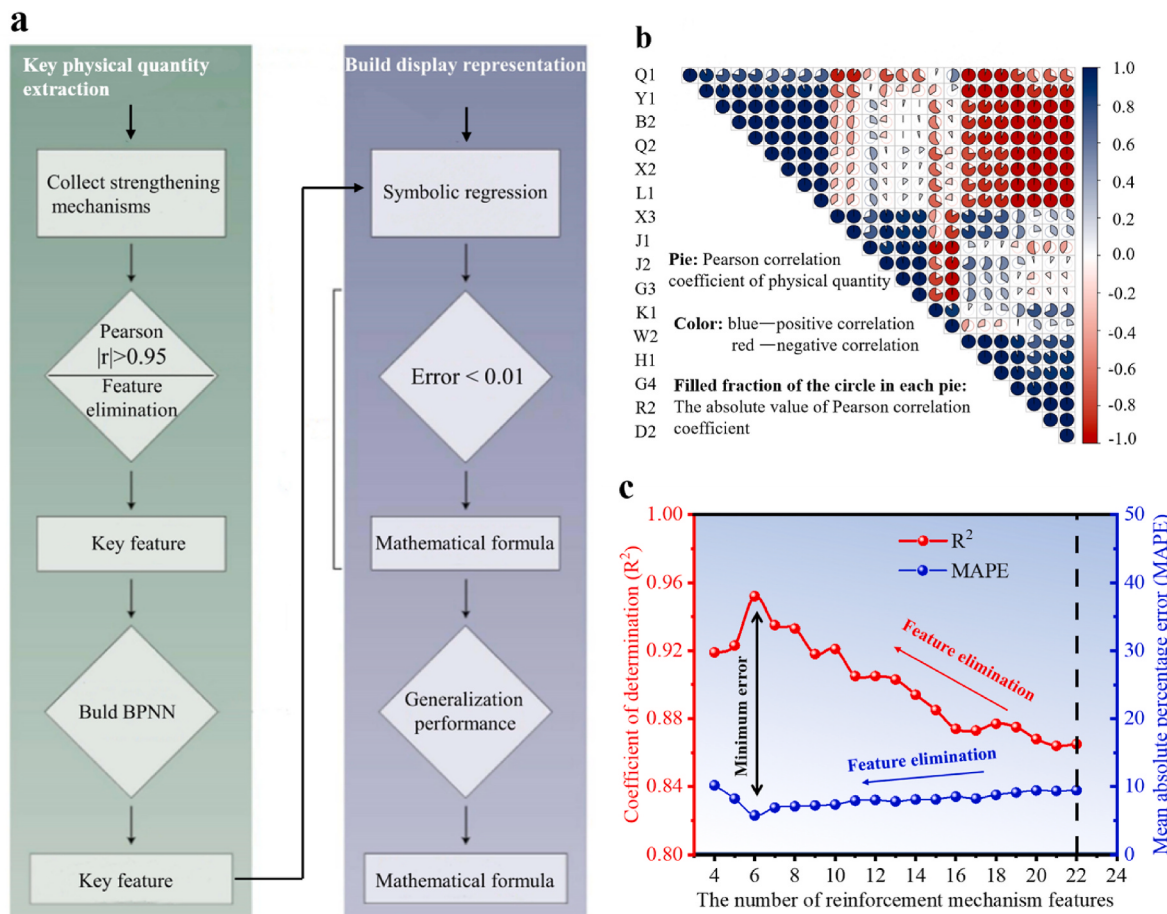


**Fig. 3.** The process of determining the key feature subset. (a) The research route of this work. (b) The preliminary selection enhancement mechanism based on Pearson correlation. (c, d) Further narrowing the subset based on the random forest recursive elimination method, showing (c) MAPE and the change process of (d)  $R^2$ . The display expression of machine learning shows that the contribution of multiple strengthening mechanisms to yield strength is obviously not linear, so it is expressed as NL-RR. The linear relationship is represented by L-RR.

mapping relationship of BPNN can further determine whether the key physical quantities screened carry the main characteristics of YS. The generalization performance of machine learning frameworks is validated through multiple heterogeneous structured materials data, including electroplated gradient nanotwinned Cu [55], gradient high-entropy alloy prepared by surface mechanical deformation [56], and thermomechanically processed ultrafine-grained carbon steel (i.e., ultrafine globular structure) [33,34].

Using the method of Benesty et al. (2009) to screen the 25 strengthening mechanisms linearly through the Pearson coefficient, the purpose is to eliminate redundant and theoretically excessive physical quantities. Eq. (10) can be used to calculate the correlation  $r$  between any two physical quantities. When the absolute value of  $r$  is greater than 0.95, it is considered that there is a strong correlation between the two strengthening mechanisms, as shown in Fig. 3(b).

After the simple and quick screening, W2, G3, and K1 were excluded, and 22 strengthening mechanisms were finally identified (Supplementary material). However, establishing an intuitive mathematical expression of the relationship is still relatively complex. To this end, we define a random forest classifier in Python, including the evaluation of feature indices and accuracy scores. One of the 22 strengthening mechanisms is taken out one by one, and the remaining parameters are used as the input of the random forest algorithm, and 22 models with different parameters can be obtained. By repeating the entire recursive process, the importance score of the feature can be calculated. Scores are represented using mean absolute percent error (MAPE) and coefficient of determination ( $R^2$ ). The deviation in MAPE is absolute, and there will be no positive and negative offsets, which can better reflect the actual situation of the predicted value (the smaller the value, the better the accuracy of the prediction model).  $R^2$  is the basic index rating coefficient for visually judging the degree of model fitting. The closer the value is to 1, the better the model fit.

It can be seen from Fig. 3(c and d) that as the recursion proceeds, the accuracy of the model first increases and then decreases. The best accuracy is obtained when the strengthening mechanism is 6, the model can evaluate  $\sim 95\%$  of the data relatively accurately, and the MAPE value is 8.21%. The six key physical quantities are grain boundary strengthening ( $\sigma_g$ ), dislocation strengthening ( $\sigma_d$ ), second phase strengthening ( $\sigma_{Orowan}$ ), back stress strengthening ( $\sigma_{HDL}$ ), solid solution strengthening ( $\sigma_s$ ), and lattice intrinsic friction strengthening ( $\sigma_f$ ). Based on metallurgical principles, a rational analysis of the data statistically obtained can be conducted. Solid solution strengthening results from the dissolution of solute atoms in the metal matrix, providing a stable strengthening effect that is not significantly affected by variations in strain range. Additionally, under constant strain rate conditions, the lattice friction resulting from atomic interactions within the lattice can be treated as a constant, remaining relatively unchanged. Therefore, the effects of these two strengthening mechanisms are stable and insensitive to other mechanisms, allowing for a unified consideration that results in minor impact and a streamlined classification into five strengthening mechanisms. This work focuses on the coupling between the strengthening mechanisms brought by the new structure, allowing the direct equivalence of the two mechanisms to be  $\sigma_0$ , equivalent to five characteristics.

### 3.2. Build strengthening relationships

To further determine whether the selected parameters contain the key information describing YS, 5 kinds of features are used as the input of BPNN, and YS is used as the output. The network structure of BPNN is determined by cross-validation.

The hyperparameters of BPNN include the number of network layers, the number of neurons, the activation function, and the learning rate. It is proved that for metal materials, the three-layer, four-layer, or five-layer network structure can basically achieve an excellent fitting effect. The number of neuron nodes is selected according to the Hecht-

Nelson method [57], as shown in Eq. (11).

$$m = 2n + 1 \quad (11)$$

The number  $n$  of neurons in the input layer is 5, and the number  $m$  of neurons in the hidden layer is 11. The correct selection of the activation function can achieve a good nonlinear mapping and authenticity approximation. The activation function of the output layer is usually a linear direct output, so the Purlin function ( $F_1$ ) is chosen, as shown in Eq. 12–14. We select hidden layer activation functions from Sigmoid ( $F_2$ ), Tanh ( $F_3$ ), and Purlin functions respectively.

$$F_1 = x \quad (12)$$

$$F_2 = \frac{1}{1 + e^{-x}} \quad (13)$$

$$F_3 = \frac{e^x - e^{-x}}{e^x + e^{-x}} \quad (14)$$

where  $x$  is the input signal. Under the condition that  $m$  is kept constant, the same sample set is used for training. When the number of hidden layers is 1, 2, and 3, respectively, the experimental steps are shown in Table 1 and Table 2, and each hidden layer is named M, N, and F, respectively. Since the number of experiments required is too many when the number of hidden layers is 3, a three-factor and three-level orthogonal experiment ( $L_9 3^3$ ) is designed as shown in Table 2.

Under the condition that other parameters of the network remain unchanged, the same sample set is used for training, and the error characteristics and training steps corresponding to each group of training are obtained, as shown in Fig. 4. It can be seen from Fig. 4(a–c) that BPNN shows excellent prediction accuracy when training the data of CG, NFG/NG, and HSMs indiscriminately (Most of the schemes in Tables 1 and 2 have lower MAPE values relative to linear theory). However, for the performance of the BP network, there is an optimal combination of the number of hidden layers and the activation function, which makes the prediction accuracy the highest and the number of training steps minimum. In the structure with 4 layers of neurons (input layer, hidden layer M – N, and output layer), when the activation function of the hidden layer M – N is  $F_{2-2}$ , the prediction accuracy is the highest and the number of training steps is the lower, the MAPE is 5.36%, and the number of training steps is 14 (Fig. 4(b)). After continuing to add the hidden layer F, the prediction accuracy drops significantly, and the change of the activation function will cause a large fluctuation in the prediction accuracy, making it easier to fall into a local minimum or overfitting. Therefore, the network structure of BPNN is determined to be  $5 \times 11 \times 11 \times 1$  (the two activation functions are Sigmoid and Purlin). Finally, it can be confirmed that the selected five key physical quantities can be used to describe the characteristics of yield strength. Therefore, the network structure of BPNN is determined to be  $5 \times 11 \times 11 \times 1$  (the three activation functions are Sigmoid, Sigmoid, and Purlin). Finally, it can be confirmed that the selected five key physical quantities can be used to describe the characteristics of yield strength.

The hidden layer uses the Sigmoid function to non-linearly map the data to the output layer, and the activation function of the output layer is Purlin, finally, a  $5 \times 11 \times 11 \times 1$  network structure is obtained (Fig. 5(a)). Fig. 5(b) shows that nonlinear BPNN has high prediction accuracy

**Table 1**

When the number of hidden layers is 1,  $F_1$ ,  $F_2$ , and  $F_3$  activation functions (AF) are selected for training respectively.

| Experiment no. | AF <sub>M</sub> |
|----------------|-----------------|
| 1              | $F_1$           |
| 2              | $F_2$           |
| 3              | $F_3$           |

**Table 2**

BPNN has training schemes with 2 and 3 hidden layers, among which, the 3 hidden layers are designed for  $L_9 3^3$  cross-experimental design. The combination of activation functions  $F_1$  and  $F_2$  is represented by  $F_{1 \rightarrow 2}$ , the combination of activation functions  $F_1$ ,  $F_2$ , and  $F_3$  is represented by  $F_{1 \rightarrow 2 \rightarrow 3}$ , and so on.

| Experiment no. | $AF_{M-N}$            | $AF_{M-N-F}$                        |
|----------------|-----------------------|-------------------------------------|
| 1              | $F_{1 \rightarrow 1}$ | $F_{1 \rightarrow 1 \rightarrow 1}$ |
| 2              | $F_{1 \rightarrow 2}$ | $F_{1 \rightarrow 2 \rightarrow 2}$ |
| 3              | $F_{1 \rightarrow 3}$ | $F_{1 \rightarrow 3 \rightarrow 3}$ |
| 4              | $F_{2 \rightarrow 1}$ | $F_{2 \rightarrow 1 \rightarrow 2}$ |
| 5              | $F_{2 \rightarrow 2}$ | $F_{2 \rightarrow 2 \rightarrow 3}$ |
| 6              | $F_{2 \rightarrow 3}$ | $F_{2 \rightarrow 3 \rightarrow 1}$ |
| 7              | $F_{3 \rightarrow 1}$ | $F_{3 \rightarrow 1 \rightarrow 3}$ |
| 8              | $F_{3 \rightarrow 2}$ | $F_{3 \rightarrow 2 \rightarrow 1}$ |
| 9              | $F_{3 \rightarrow 3}$ | $F_{3 \rightarrow 3 \rightarrow 2}$ |

(MAPE is 5.36%,  $R^2$  score is 0.97), which verifies the accuracy of the selected key subset.

When using the L-RR to describe the CG dataset (Eq. (15)), the MAPE value is 3.46% (Fig. 5(a and b)), and the  $R^2$  score is 0.98. Since the grain surface area of NG/UFG is larger relative to the volume, the scale coefficient of surface atoms is higher, and the corresponding interface defects and grain boundary defects will also increase. As a result, when the linear strengthening rule fits the NG/UFG dataset (Fig. 5(c)), it can cover about 90% of the data, and the MAPE value increases to 13.42%. HSMs often contain different phases, and they can vary in size, shape, composition, and arrangement. The interactions generated by the spatial heterogeneity of these different structures have a great influence on the

behavior of materials such as lattice defects, grain boundaries, dislocations, and interphase shearing. These complex interactions make the mechanical behavior of HSMs difficult to describe by traditional linear strengthening methods (Fig. 5(d)), leading to a significant increase in the MAPE value to 16.23% and a decrease in the  $R^2$  score to 0.81.

$$YS = \sigma_0 + \sigma_g + \sigma_d + \sigma_{Orowan} + \sigma_{HDI} \quad (15)$$

$$YS = a\sigma_0 + b\sigma_g + c\sigma_d + d\sigma_{Orowan} + e\sigma_{HDI} \quad (16)$$

When plastic deformation occurs in the material, the influence of local structure and energy states may lead to the predominance of one or several strengthening mechanisms. To consider the dominant role of strengthening mechanisms in alloys, a weighting method is applied to each mechanism, using constant terms (a, b, c, d, e) to differentiate their contributions to YS as shown in Eq. (16) [58,59]. However, from Fig. 6(a), it can be observed that the weighting method (L-RRW) is only effective within a certain range (MAPE value of 10.48% and  $R^2$  score of 0.91). It can be seen that the linear strengthening method is not suitable for complex strengthening mechanisms in NG/UFG and HSM, but to some extent, it coincides with the basic trend of YS. Therefore, introducing a bias term b in Eq. (16) to obtain Eq. (17) is necessary to adjust the deviation of the results.

$$YS = a\sigma_0 + b\sigma_g + c\sigma_d + d\sigma_{Orowan} + e\sigma_{HDI} + \theta \quad (17)$$

in the equation, a, b, c, d, and e are constants. According to the data transmission law of BPNN, Eq. (17) is then mapped non-linearly using the  $F_2$  function to obtain the following relationship:

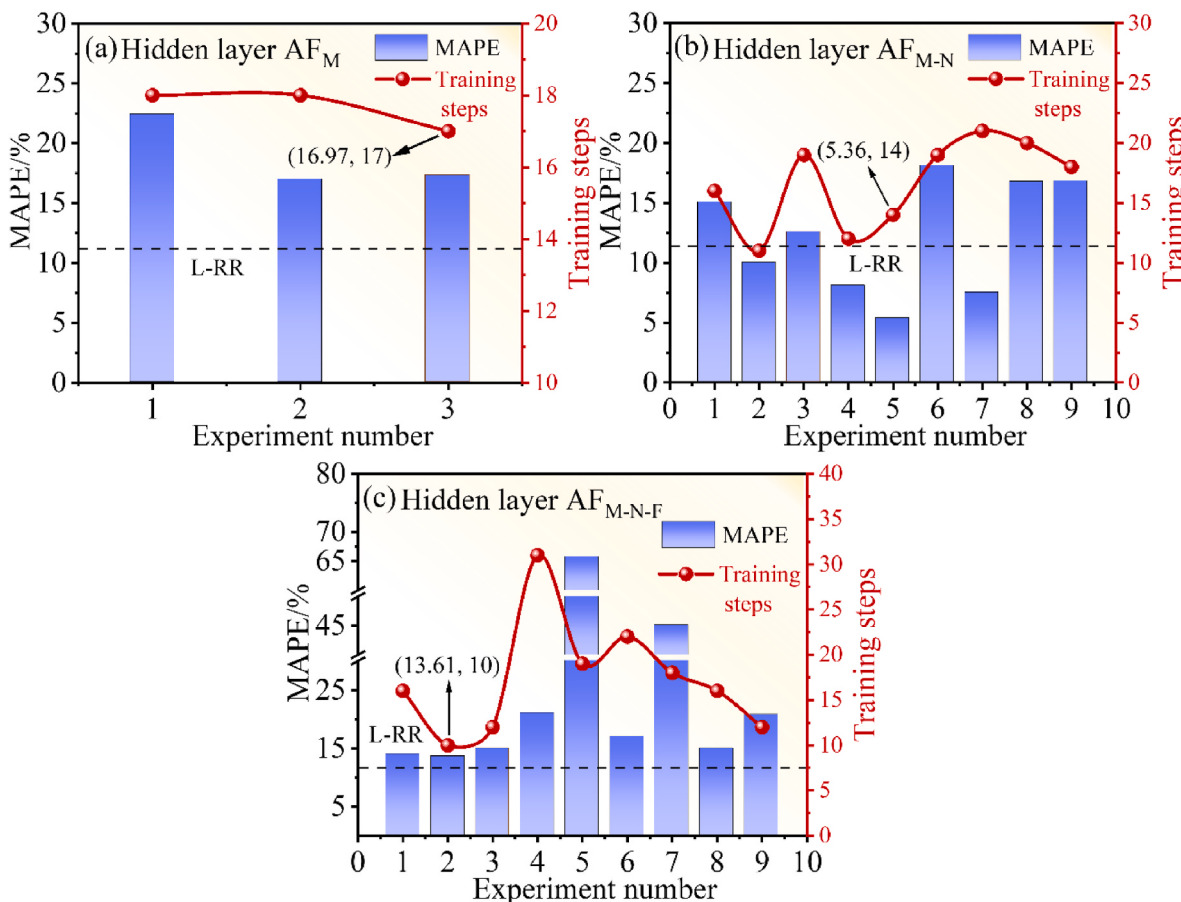


**Fig. 4.** The influence of BPNN network structure on network performance. (a) When BPNN has a hidden layer (M), the influence of activation function on network performance, the values in parentheses represent MAPE and Training steps. (b) When the BPNN has two hidden layers (M-N), the effect of the activation function on the performance of the network, it is found that the accuracy of the linear relationship  $F_{3 \rightarrow 3}$  is similar to that of the linear superposition relationship. (d) Effect of activation function on network performance when BPNN has three hidden layers (M-N-F).

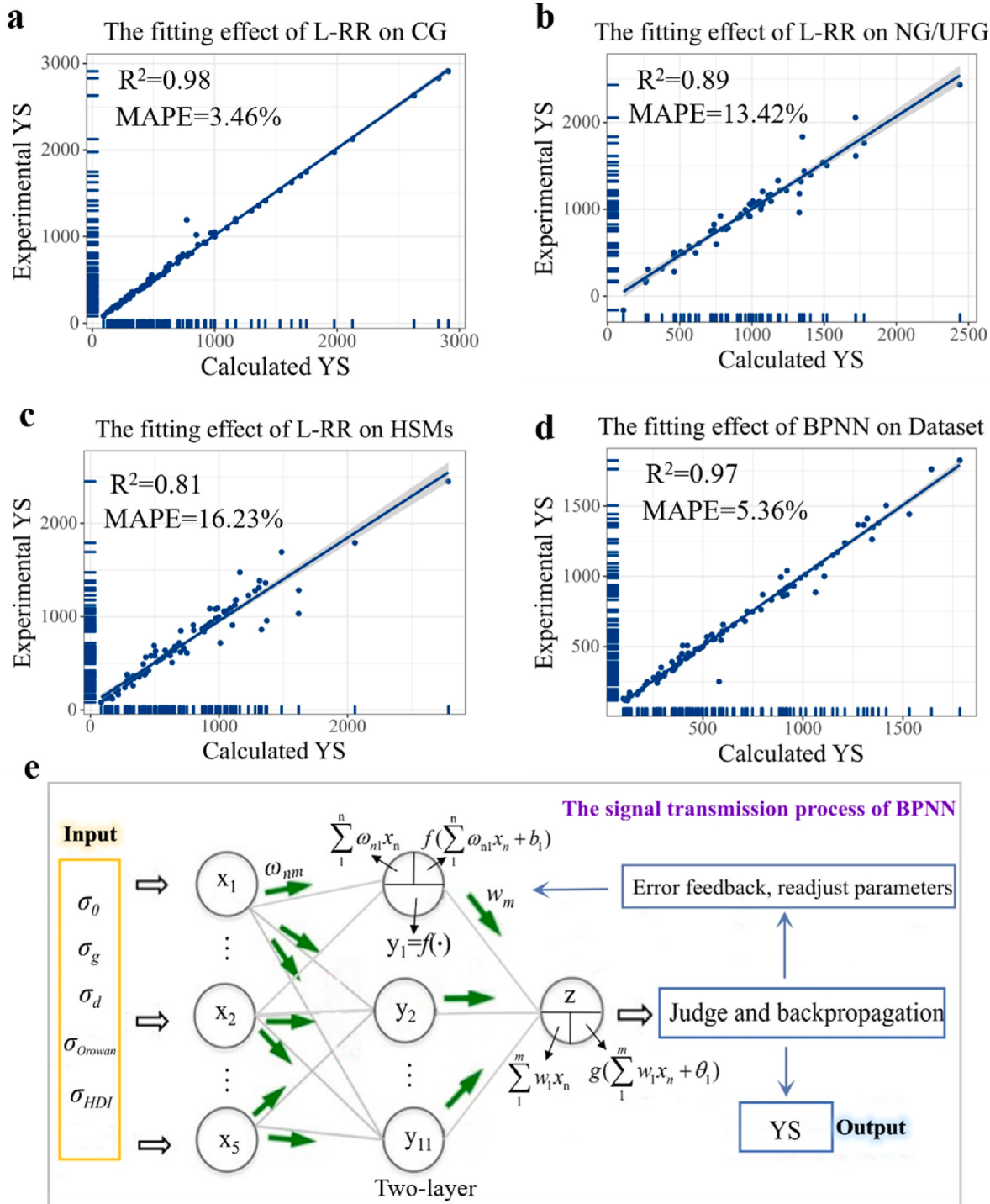


**Fig. 5.** Confirms the accuracy of key physical quantities. (a) The fitting effect of the L-RR on CG, which has excellent prediction accuracy. (b) When the L-RR fits NG/UFG materials, the prediction accuracy deviates. (d) The L-RR has a relatively large prediction error for HSMs, indicating that it does not conform to the intrinsic physical mechanism. (e) The fitting accuracy of BPNN shows that the nonlinear strengthening method is more in line with the basic strengthening characteristics of the material, and proves that the selected key physical quantities fully include the key physical information of the yield strength.

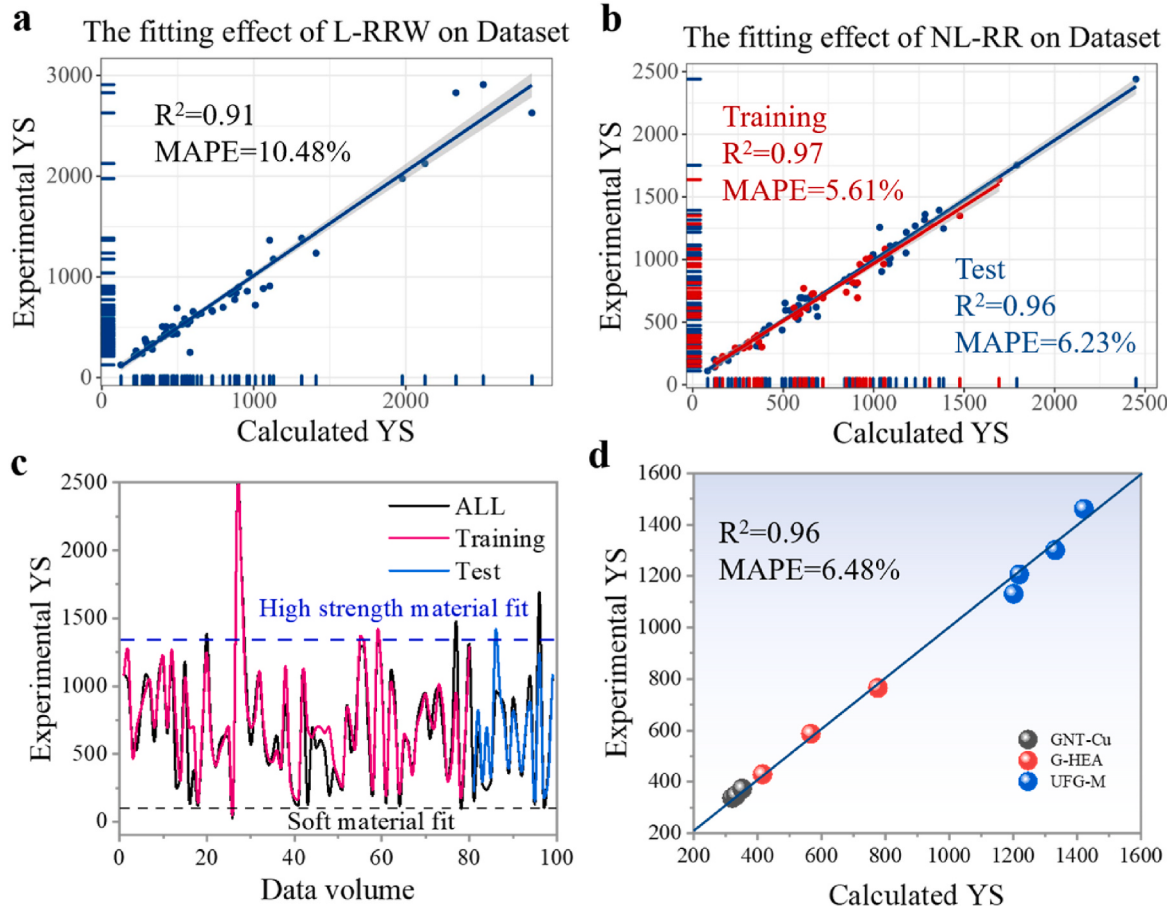


**Fig. 6.** Accuracy comparison between L-RRW and NL-RR. (a) The prediction accuracy of L-RRW is higher than that of L-RR. (b) The prediction accuracy of NL-RR is close to that of BPNN. (c) By visualizing the NL-NN prediction process, it is found that whether it is NG/UFG and HSMs with high YS or CG with low intensity, they all have a good degree of fitting. (d) Using GNT-Cu, G-HEA, and UFG -W tests NL-RR generalization ability.

$$h_1^{(1)} = F_2 \left( \omega_{11}^{(1)} \sigma_0 + \omega_{12}^{(1)} \sigma_g + \omega_{13}^{(1)} \sigma_d + \omega_{14}^{(1)} \sigma_{Orowan} + \omega_{15}^{(1)} \sigma_{HDI} + b_{ln}^{(1)} \right) \quad (18)$$

$$h_2^{(1)} = F_2 \left( \omega_{21}^{(2)} \sigma_0 + \omega_{22}^{(2)} \sigma_g + \omega_{23}^{(2)} \sigma_d + \omega_{24}^{(2)} \sigma_{Orowan} + \omega_{25}^{(2)} \sigma_{HDI} + b_{ln}^{(2)} \right) \quad (19)$$

After the second mapping using the  $F_2$  function, as shown in Eqs. 20 and 21, the final non-linear relationship (NL-RR) for yield strength, as shown in Eq. (22), based on the linear baseline rule with  $b$  is obtained.

$$h_1^{(2)} = F_2 \left( \lambda_{11}^{(2)} h_1^{(1)} + \lambda_{12}^{(2)} h_2^{(1)} + \delta_{ln}^{(2)} \right) \quad (20)$$

$$h_2^{(2)} = F_2 \left( \lambda_{21}^{(2)} h_1^{(1)} + \lambda_{22}^{(2)} h_2^{(1)} + \delta_{ln}^{(2)} \right) \quad (21)$$

$$YS = w_1 h_1^{(2)} + w_2 h_2^{(2)} + \theta_n \quad (22)$$

From Fig. 6 (b, c), it can be seen that NL-RR exhibits excellent prediction accuracy for various novel structural materials (MAPE value of 5.61% and  $R^2$  score of 0.97). NL-RR has been validated with material structure data from several works, including electro-deposited gradient nanotwinned Cu [55], surface mechanical deformation-prepared gradient high-entropy alloys [56], and warm-rolled ultrafine-grained medium-carbon steel [33,34]. It exhibits outstanding prediction accuracy and generalization performance, with a MAPE value of 6.48% and an  $R^2$  score of 0.96 as shown in Fig. 6(d). The YS of gradient nano-twinned Cu is ~10% higher than that of Cu with the same grain size [55,60]. This is due to the interaction between gradient grain boundaries and back stress, and gradient medium entropy alloys have similar structural characteristics and mechanical behavior. For the

near-equi-axed organization of medium-carbon steel with an average grain size of 5  $\mu\text{m}$ , its strengthening mechanism is the same as that of plain medium-carbon steel [33]. However, due to the strengthening effect of dispersed ferrite on grain boundaries, YS increases from ~345 MPa to ~1200 MPa [34], which significantly exceeds the predicted value by L-RR.

It can be concluded that our proposed NL-RR has excellent cross-scale and cross-structure prediction capabilities and generalization performance. This data-driven approach provides insights for micro and even macrostructure design.

Under the assumptions of the methodology described in Section 2.1, the predictive accuracy obtained from the nonlinear relationship is already close to the true yield strength of materials with non-uniform microstructures. The error in the linear relationship mainly arises from the coupling effects caused by multiple strengthening mechanisms. By excluding errors from data statistics and crystal plasticity theory, the coupling strengthening effect can be directly calculated by subtracting the nonlinear relationship from the linear relationship.

### 3.3. Physical meaning analysis

We have successfully implemented a quantitative representation of a novel YS strengthening mechanism, which preserves certain characteristics of L-RR while accounting for the coupling effects induced by interactions. This contributes to the understanding of complex scenarios such as long-distance dislocation motion in composite structures. The yielding of the material is related to the initiation and propagation of dislocations. When the dislocation starts, the nearby atoms continuously

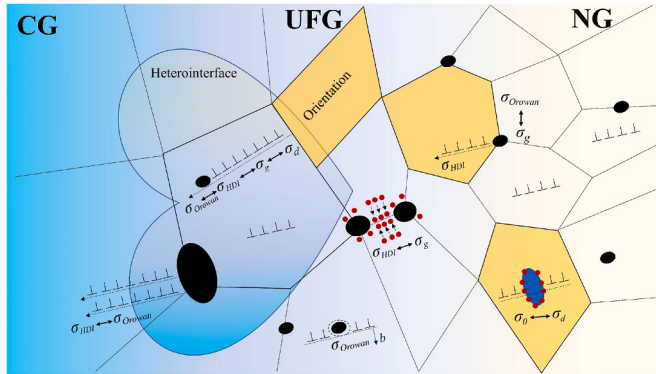


**Fig. 7.** Illustration of the interactions between key strengthening mechanisms in CG, NG, and UFG materials, showcasing the coupling effects of second phase and heterogeneous boundaries that promote long-range stress relaxation, second-phase strengthening at grain boundaries, formation of sub-grain boundaries induced by the second phase, and hindered dislocation motion due to lattice distortion. In the diagram, black circles represent second-phase particles, T-shaped symbols represent dislocations, and red dots represent atoms. The presentation here is an improvement on previous work ref. [61]. (For interpretation of the references to colour in this figure legend, the reader is referred to the Web version of this article.)

interact with the matrix along the Burgers vector direction on the slip plane. Lattice friction, as an interaction force between atoms, first acts on dislocations. In addition to causing lattice distortion, lattice friction exerts an opposing force on the dislocation, making it more difficult for the dislocation to move. This resistance can cause dislocations to twist

and buckle in the crystal, which is related to the dislocation density and the degree of lattice distortion, and has an auxiliary effect on the dislocation-strengthening mechanism. Similar to it is the solid solution lattice. The interaction between dislocations and grain boundaries has been studied in depth. The accumulation and absorption of dislocations at grain boundaries result in the formation of sub-angle grains, leading to stronger grain boundary strengthening (Fig. 7). The sub-grain boundaries where dislocations are arranged in a specific way will form a high-angle grain boundary partition matrix during the continuous absorption of dislocations, leading to stronger grain boundary strengthening, such as our previous work Ref. [61] (Fig. 7). At this time, under the effect of such dislocation strengthening, the density of sub-angle grains, low-angle grain boundaries and high-angle grain boundaries are increased, which promotes grain boundary strengthening.

### 3.4. Strengthening mechanisms of eutectic high-entropy alloys

Inspired by the aforementioned physical significance, an attempt was made to optimize the structure and mechanical properties of the AlCoCrFeNi<sub>2.1</sub> eutectic high-entropy alloy (EHEA) by elucidating its strengthening mechanisms based on linear and nonlinear strengthening relationships. Shi et al. (2021) utilized the directional solidification or cold rolling methods to fabricate lamellar high-strength eutectic high-entropy alloys, where the coordinated strength and toughness arise from the coupling of multiple strengthening mechanisms. Wani et al. (2016) achieved enhanced strength and toughness in eutectic high-entropy alloys by cold deformation to create a typical heterogeneous structure. Transmission electron microscopy (TEM) revealed that this

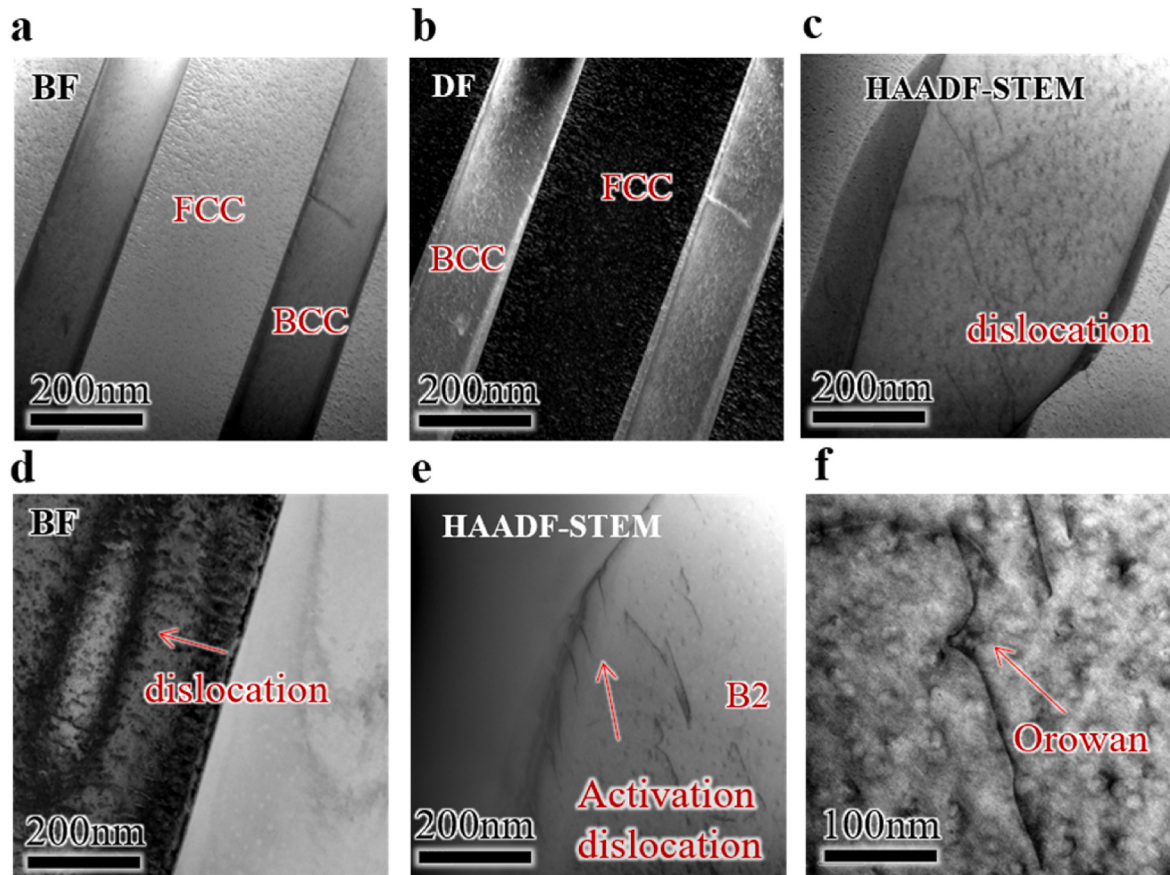


**Fig. 8.** Strengthening mechanism of AlCoCrFeNi<sub>2.1</sub> alloy. (a) Bright-field image. (b) Dark-field image. (c) HAADF-STEM observation of sites in the BCC matrix dislocations. (d) Found that dislocations are distributed along the boundaries of BCC and FCC. (e) Using HAADF-STEM, it was observed that dislocations precipitated from the BCC/FCC heterogeneous boundary to the BCC boundary. (f) The Orowan relationship between dislocations and cementite mechanism.

improvement was attributed to the combination of soft and hard domains. Currently, the fundamental toughening mechanism of the AlCoCrFeNi<sub>2.1</sub> eutectic high-entropy alloy remains insufficiently understood.

We first investigated the microstructural characteristics of the material using transmission electron microscopy (TEM), scanning electron microscopy (SEM), and electron backscatter diffraction (EBSD). The multiple mechanical coupling responses of the material were quantitatively calculated based on the structural parameters and nonlinear coupling terms. As shown in Figs. 2 and 8, the initial state of the as-cast AlCoCrFeNi<sub>2.1</sub> eutectic high-entropy alloy (AC) exhibited strip-shaped or curved L1<sub>2</sub> and B2 phases, which alternately arranged similarly to a lamellar pearlite structure. The B2 phase was rich in Al and Ni elements, while the L1<sub>2</sub> phase was stabilized by Cr, Fe, and Ni elements. The yield strength of the AC sample is 384 MPa, the ultimate tensile strength is 1046 MPa, and the elongation is 16% (Fig. 9). The grain boundary strengthening effect was calculated based on the characterization details and the Hall-Petch relationship (Eq. (23)), yielding approximately 98 MPa (Fig. 10).

$$\sigma_g = kS_{EHEA}^{-1/2} \quad (23)$$

$k$  represents a proportionality constant.  $S$  denotes the average inter-lamellar spacing between the B2 and L1<sub>2</sub> phases, which was statistically measured using Image Pro software.

In the plastic deformation process of polycrystalline materials, the density of dislocations is directly related to the yield strength. The L1<sub>2</sub> phase, as a soft FCC phase, is alternately arranged with the relatively hard B2 phase. Under low stress, dislocations were emitted at phase interfaces (Fig. 8), migrated within the L1<sub>2</sub> phase between the two hard phases under the action of stress  $\tau$ , and piled up at adjacent lamellar interfaces [62,63]. This phenomenon was particularly significant between lamellar interfaces parallel to the loading axis. Under higher stress, the accumulated dislocations in lamellar layers parallel to the loading axis contributed to a strong shear effect. When the shear force exceeded a certain threshold, the dislocations began to break the constraints of the phase boundaries and continued to propagate. The contribution of dislocation density to the yield strength of the lamellar EHEA was quantified using the Bailey-Hirsch relationship [64], as shown in Eq. (24), indicating a dislocation strengthening value of approximately 153 MPa for the AC sample (Fig. 10). Dollar et al. (1988) quantified  $\tau$  using Eq. (25) and observed intense shear bands within the lamellar structure parallel to the loading axis, demonstrating that shear bands were the main cause of cracking in the hard phase lamellar layers.

$$\sigma_d = \alpha GM\rho^{1/2} \quad (24)$$

$$\tau = \frac{AGb}{2\pi V_{FCC}} \ln \left( \frac{S_{EHEA} V_{FCC}}{b} \right) \quad (25)$$

where  $\alpha$  is a constant with a value of 0.2.  $G$  represents the shear modulus (150 GPa), and  $b$  stands for the Burgers vector.  $M$  is the Taylor factor.  $\rho$  is the dislocation density. TEM analysis showed that the average dislocation density of the fractured specimens of AC, A600, A700, and A800 was about  $2.89 \times 10^{15}/m^2$ ,  $1.93 \times 10^{16}/m^2$ ,  $1.58 \times 10^{16}/m^2$ , and  $8.22 \times 10^{15}/m^2$ , respectively.  $V_{FCC}$  represents the volume fraction of the L1<sub>2</sub> phase. For screw dislocations,  $A$  is equal to 1. For edge dislocations,  $A$  is equal to  $1/(1-v)$ , where  $v$  is the Poisson's ratio. For mixed dislocations,  $A$  is equal to 1.21.

The yield strength of the lamellar structured EHEA depended on the lamellar spacing, and intense shear bands only appeared at regions with larger interlamellar spacings and growth defects, while the occurrence frequency of shear bands within thin lamellar layers was low. The AC sample was mainly composed of large area phase boundaries (approximately 92%) with only a small number of conventional grain boundaries (Fig. 1). Therefore, theoretically, when  $\tau > \sigma_g$ , the phase boundary will be disrupted. In other words, when  $\frac{\tau}{\sigma_g} > 1$ , dislocations will induce crack initiation at the interface, as represented by Eq. (26).

$$\frac{\tau}{\sigma_g} = \frac{\frac{AGb}{2\pi V_{FCC}} \ln \left( \frac{S_{EHEA} V_{FCC}}{b} \right)}{kS_{EHEA}^{-1/2}} \quad (26)$$

It can be observed that controlling the interaction between dislocations and interfaces through methods such as nanoscale lamellar structures, increased phase boundary density, and modified interface curvature is a way to enhance the yield strength. This is demonstrated by the work of Ren et al. (2022b), who achieved high strength and toughness in EHEA by refining the lamellar microstructure and increasing the density of phase boundaries through additive manufacturing [65,66].

It is well known that the accumulation of geometrically necessary dislocations (GNDs) arrays at interfaces can release long-range internal stresses, leading to heterogeneous deformation-induced (HDI) high stress and additional grain boundary strain hardening, thereby enhancing the strength and ductility of heterogeneous structure materials. Similar to other heterogeneous structure materials, the accumulation of GNDs at the heterogeneous boundaries of AC causes a certain level of HDI stress. During plastic deformation, the softer L1<sub>2</sub> phase is

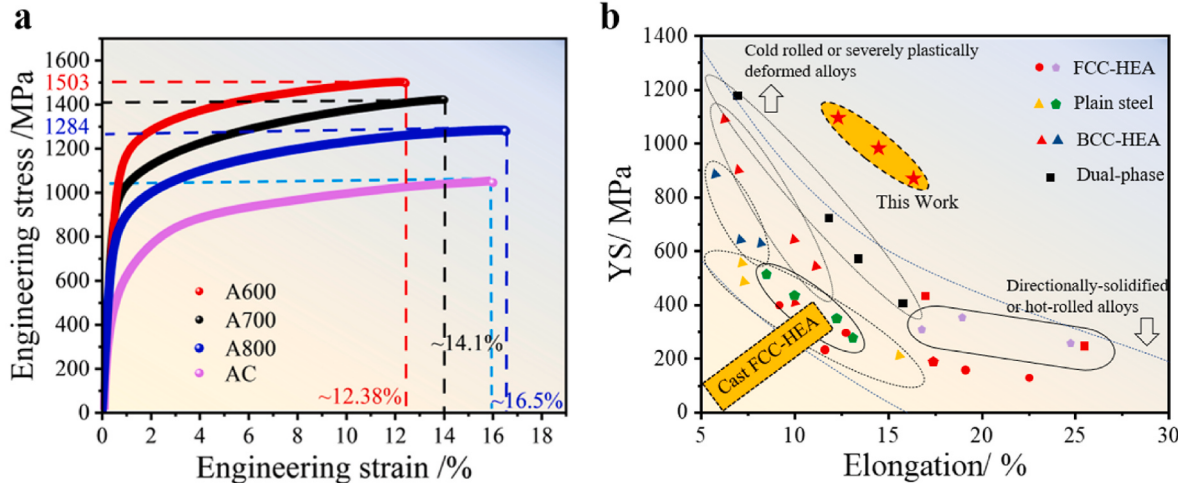
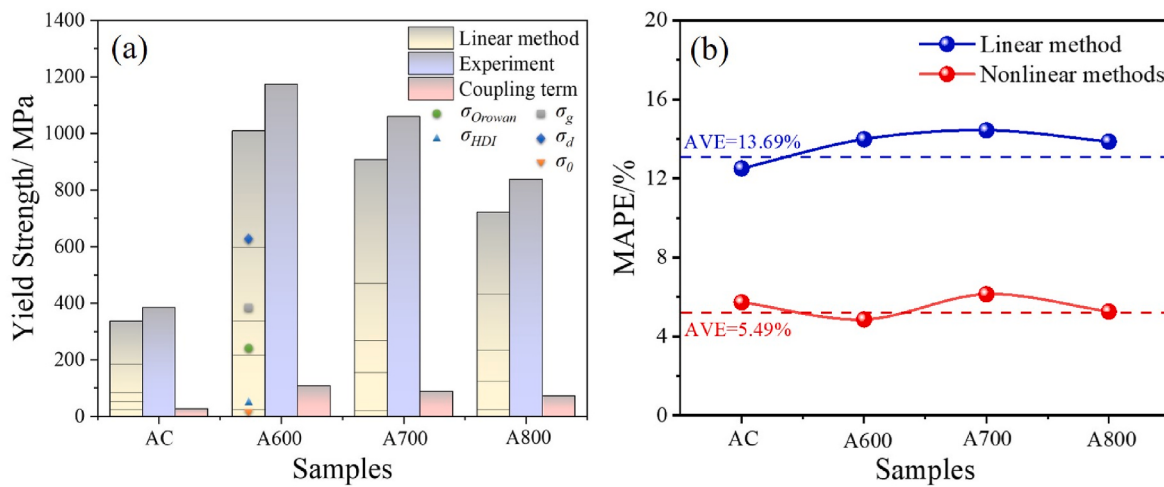


Fig. 9. The mechanical properties of the AlCoCrFeNi<sub>2.1</sub> alloy are shown in (a) as the engineering stress-strain curve and in (b) as the distribution of mechanical properties.



**Fig. 10.** Yield strength estimation of eutectic high-entropy alloys using linear strengthening method and introducing nonlinear strengthening term method. (a) Quantitative and predicted values of the main strengthening mechanisms in eutectic high-entropy alloys. The linear method shows a certain degree of underestimation, which can be compensated by introducing nonlinear terms. (b) MAPE values of the linear method and the nonlinear method.

constrained by the harder B2 phase, gradually transferring stress from the L1<sub>2</sub> phase to the B2 phase, thereby utilizing mechanisms such as grain boundary strengthening and HDI stress [67]. Referring to the method employed by Du et al. [68,69], the HDI stress was quantified (Eq. (27)), yielding approximately 103 MPa. Additionally, we observed the presence of a high density of coherent nanoscale precipitates in this EHEA, with strong interactions between dislocations and nanoscale precipitates in both eutectic B2 and L1<sub>2</sub> phases. The HDI stress, acting in the opposite direction of the dislocation motion, and the Orowan stress induced by coherent nanoscale precipitates (Eq. (28)) directly reduce the stress concentration of dislocations at phase boundaries. As a result, Eq. (26) and the phase boundary stability inequality ( $\frac{\tau}{\sigma_g} > 1$ ) can be modified to Eq. (29), reducing the shear stress caused by the accumulation of dislocations at phase boundaries.

$$\rho_{GND} = 2\theta/\mu b \quad (27)$$

$$\sigma_{Orowan} = 1.19 \frac{T}{Rb} f^{1/2} \quad (28)$$

$$\frac{\tau - \sigma_d - \sigma_{HDI} - \sigma_{Orowan}}{\sigma_g} = \frac{\frac{AGb}{2\pi V_{FCC}} \ln\left(\frac{S_{EHEA}V_{FCC}}{b}\right) - \alpha GM\rho^{1/2} - 1.19 \frac{T}{Rb} f^{1/2}}{kS_{EHEA}^{-1/2}} \quad (29)$$

in the equation,  $\mu$  represents the scanning step size in electron back-scatter diffraction (EBSD).  $\theta$  is the average kernel average misorientation (KAM) obtained through EBSD statistics. T is the line tension of dislocation lines, R represents the radius of precipitate particles, and f denotes the volume fraction of the particles.

According to the above results, the AC sample exhibits an easy occurrence of slip-induced dislocation in the FCC (L1<sub>2</sub>) soft phase and a reinforcing effect in the BCC (B2) hard phase. They are arranged in alternating parallel layers, forming the lamellar heterogeneous microstructures. In addition, some coarse B2 plates and island-like structures are observed. According to the study by Gao et al. [70], the soft/hard phase lamellar heterogeneous structure occurs preferentially in the softer soft phase during the early yielding stage, constrained by the adjacent hard phase. This significantly strengthens the soft phase, making it almost as strong as the hard phase. Therefore, the tensile strength of the non-uniform heterogeneous structure is higher than the value predicted by the linear rules [70]. Additionally, due to the lower strain-hardening ability of the B2 hard phase, strain localization occurs earlier in the hard phase, with the adjacent L1<sub>2</sub> soft phase providing constraint. This mutual constraint results in strain gradient

accumulation near the L1<sub>2</sub>/B2 phase interface (Fig. 8(a–e)). The deformability of the soft and hard phases is different, resulting in strain/stress incompatibility between them. As different strains are borne by the adjacent hard and soft phases, strain gradients should exist near their interface. As deformation continues, the strain gradient increases. To accommodate the accumulated strain gradient, a large number of geometrically necessary dislocations (GNDs) accumulate at the interface, forming high back stresses, thus significantly improving the processing hardening ability of AC. To activate new dislocations, the long-range stress field induced by the back stresses must be overcome, requiring higher stress loading. Therefore, the advantage of the lamellar structure lies in the strain incompatibility provided by the soft/hard phases (i.e., inducing the HDI mechanism) and the synergistic effect between the classic dislocation strengthening mechanism and the grain boundary strengthening mechanism, thereby delaying the occurrence of necking during the strain process in AC lamellar heterogeneous samples, while balancing strength and ductility.

According to the obtained linear superposition rules for calculating all the structural parameters of the yield strength of EHEA, it was found that the estimated value for the yield strength of the AC sample is approximately 336 MPa, resulting in an underestimation of 48 MPa with a MAPE of approximately 12.5%. To clarify the source of this error, we supplemented the experimental details. If there is a significant difference in the mechanical properties between the soft and hard phases, the phase boundaries will exhibit severe lattice mismatch effects due to heterogeneity. High-resolution transmission electron microscopy (HRTEM) revealed the presence of a semi-coherent interface with low lattice mismatch (Fig. 11(b)) between the eutectic L1<sub>2</sub> and B2 phases, which contributes to stabilizing the eutectic phase. In Fig. 11(b and c), an ordered lattice arrangement was observed at the phase boundaries, forming a new periodic superlattice structure, which may be the cause of the low lattice mismatch at the phase boundaries. The local lattice shear effect has been observed (Fig. 11(d and e)). Energy-dispersive spectroscopy (EDS, Fig. 11(a–f)) combined with transmission electron microscopy revealed that the semi-coherent phase boundaries are a result of strong interactions between solute elements and grain boundary defects, which compensate for the weak bonding properties caused by the lattice mismatch at the interface and reduce the tendency for cracking at the eutectic phase boundaries during deformation. This solute strengthening and grain boundary interaction were not considered in the linear rules, leading to the underestimation. Based on Eq. (29), the aforementioned strengthening effects related to solute and lattice factors at the interface were reconsidered, and Eq. (30) was obtained by

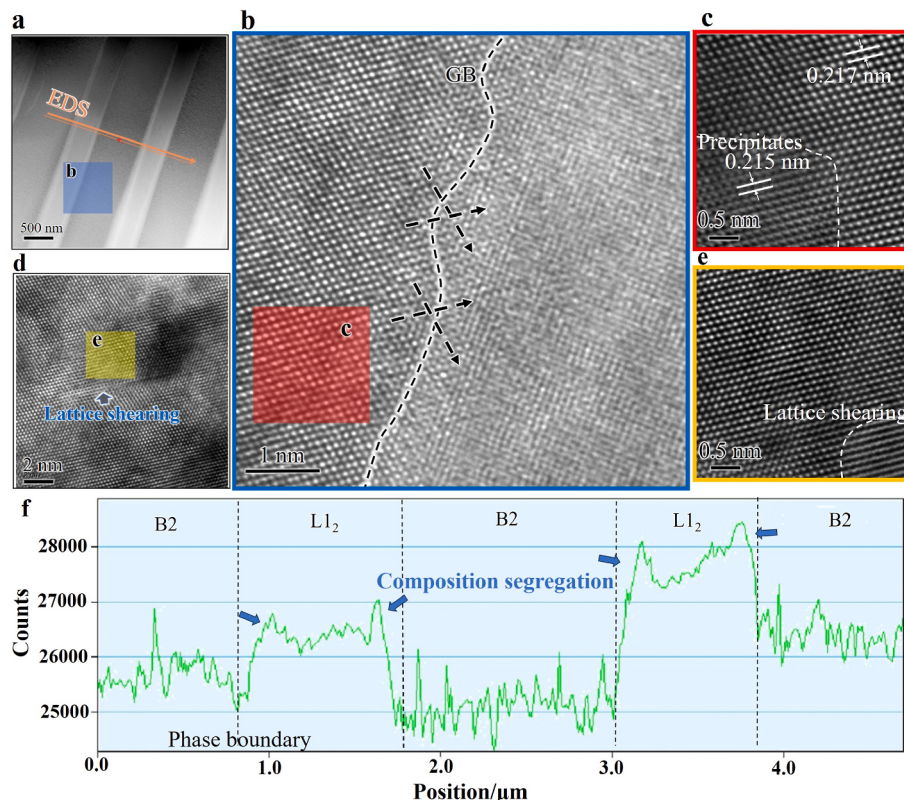


**Fig. 11.** Phase boundary structure diagram of AlCoCrFeNi2.1 alloy. (a) HAADF-TEM microstructure. (b) HRTEM image of the contact surface. (c) is the partial HRTEM magnified picture in (b), observing the matrix lattice structure and precipitated phase structure. (d) and (e) Local lattice shear bands are observed. (f) TEM-based EDS analysis reveals compositional segregation and gradient distribution at the phase boundary.

weighting each strengthening mechanism. The non-linear strengthening term (Eq. (31)) was introduced by incorporating the shear modulus to estimate the additional strengthening effect induced by the semi-coherent phase boundaries, which was approximately 26 MPa. The MAPE of the non-linear strengthening relationship was lower than that of the linear rules, at 5.73% (The yield strength of AC is estimated to be 362 MPa).

$$\frac{\tau - \sigma_d - \sigma_{HDI} - \sigma_{Orowan}}{\sigma_g + \sigma_0} = \frac{\frac{AGb}{2\pi V_{FCC}} \ln\left(\frac{S_{EHEA}V_{FCC}}{b}\right) - \alpha GM(\rho_{SSD}^{\frac{1}{2}} + \rho_{GND}^{\frac{1}{2}}) - 1.19 \frac{T}{Rb} f^{1/2}}{kS_{EHEA}^{-1/2} + \sigma_0} \quad (30)$$

$$K \frac{\tau - \sigma_d - \sigma_{HDI} - \sigma_{Orowan}}{\sigma_g + \sigma_0} = K \frac{\frac{AGb}{2\pi V_{FCC}} \ln\left(\frac{S_{EHEA}V_{FCC}}{b}\right) - \alpha GM(\rho_{SSD}^{\frac{1}{2}} + \rho_{GND}^{\frac{1}{2}}) - 1.19 \frac{T}{Rb} f^{1/2}}{kS_{EHEA}^{-1/2} + \sigma_0} \quad (31)$$

in the equation, the material constant K is used to adjust the applicability of the equation. According to the deformation Eq. (31) of the phase boundary stability inequality, it contains the relationship between multiple strengthening mechanisms, which helps to analyze and reveal the physical mechanism of phase boundary failure.

### 3.5. Strengthening mechanisms of spherical eutectic high-entropy alloys

Based on the design experience of pearlitic steels, the microstructure of lamellar pearlite contains numerous sharp angles and edges, which act as stress concentration points and can lead to stress concentration and fracture. EHEAs face similar mechanical and structural characteristics. In pearlitic steels, the presence of sharp angles and edges can be reduced through spheroidization treatments, transforming the lamellar carbides into spherical shapes. The spherical structure can distribute stress more evenly when subjected to external forces, reducing the tendency for stress concentration. Additionally, spheroidization treatments contribute to a more uniform distribution of carbide particles, minimizing gaps and cracks between the particles and fulfilling the topological stress transfer characteristics, thereby improving the mate-

rial's ductility. Drawing inspiration from the strain incompatibility of the soft/hard phases during plastic deformation and the optimization design approach of pearlite structure, apart from the extreme refinement of the B2 and L1<sub>2</sub> interlayer spacing, the stress transfer characteristics between the points and lines (second phase and interface) in spherical pearlitic steels can be employed to further enhance the load-bearing capacity of EHEAs.

The AC was subjected to warm rolling and brief annealing, resulting in the fragmentation of the hard B2 phase into spherical or short rod-

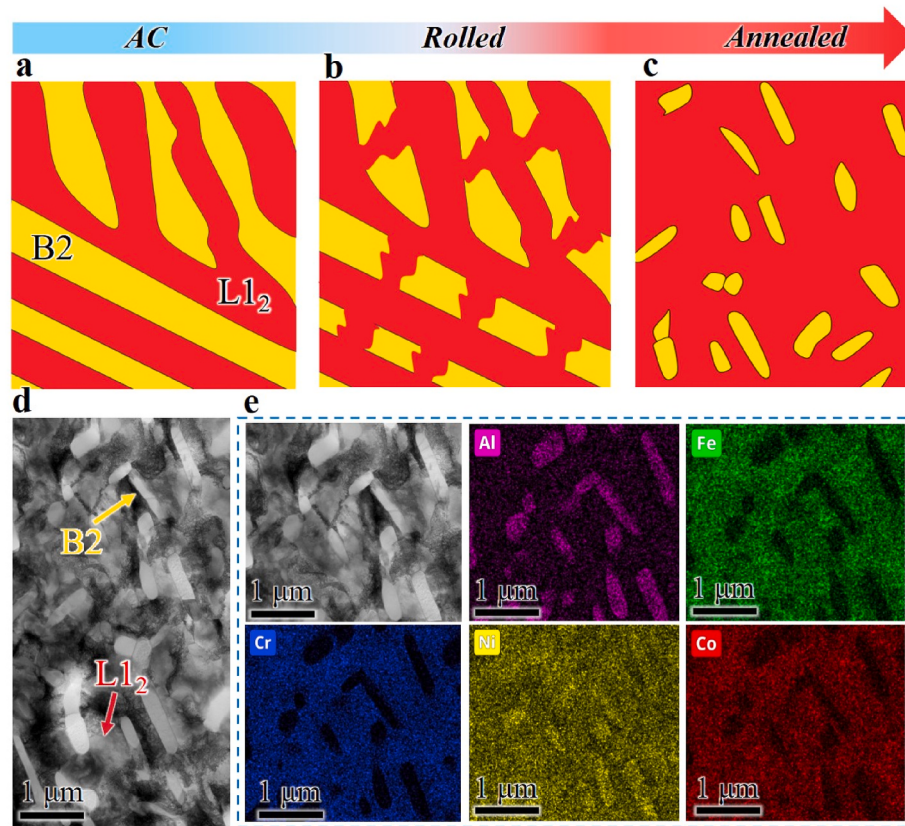


**Fig. 12.** Evolution of microstructure in the rolling and annealing processes of lamellar structures. (a–c) Schematic illustrations of microstructural evolution. (d) TEM morphology of A800. (e) EDS analysis of A800.

shaped particles dispersed within the L1<sub>2</sub> phase, forming a sample referred to as DEA (Fig. 12). The volumetric fraction of the B2 phase compared to the L1<sub>2</sub> phase remained relatively unchanged, with the B2 phase comprising approximately 33% and the L1<sub>2</sub> phase comprising around 67%. The ultrafine-grained B2 hard phase was surrounded by the softer L1<sub>2</sub> phase in a semi-coherent relationship, exhibiting a non-alternating arrangement, similar to the spheroidized pearlitic steels. However, in contrast to the spherical pearlite structure, the ultrafine-grained B2 phase contained inherently smaller coherent precipitates at the nanoscale. The ultrafine-grained L1<sub>2</sub>, ultrafine-grained B2, and nanoscale BCC precipitates constituted a multi-level composite heterogeneity with soft/hard/extrahard characteristics. The yield strength of DEA was approximately twice that of the initial state, with a negligible reduction in elongation (Fig. 9). As the rolling temperature increased and dynamic recrystallization degree enhanced, the yield strength of DEA gradually decreased (1173 MPa, 1060 MPa, 837 MPa), while the elongation increased (12.83%, 14.1%, 16.5%). The ultimate tensile strength exhibited significant improvement compared to the initial material, measuring 1503 MPa, 1410 MPa, and 1284 MPa, respectively.

The yield strength of DEA was described using both linear mixing rule and nonlinear strengthening relationships. The yield strength of DEA (A600, A700, A800) was estimated to be 1009 MPa, 907 MPa, and 721 MPa using the linear mixing rule, with an error of 13.98%, 14.43%, 13.86% (Fig. 10(b)). In contrast, the nonlinear formula yielded an error of 4.86%, 6.13%, and 5.26% in estimating the yield strength (Fig. 10 (b)). It was observed that the linear mixing rule underestimated the yield strength, with an underestimation error, while the underestimation error of the nonlinear relationship for yield strength was smaller. The graph illustrates that nonlinear quantities can significantly compensate for the underestimated portion. The excellent generalization performance of the nonlinear strengthening relationship indicates that DEA can exhibit higher strengthening mechanisms.

Quantifying additional strengthening mechanisms using nonlinear quantities helps to clarify the physical nature of the coupling of various strengthening mechanisms in DEA. The initial plastic deformation of DEA is similar to that of the AC sample, primarily driven by HDI stress, grain boundary strengthening, and dislocation strengthening. While the L1<sub>2</sub> phase is refined to an ultrafine level, its load-bearing capacity is still weaker relative to the B2 phase, exhibiting plastic deformation tendency and incompatibility of interfacial strain. Unlike the AC sample, the ultrafine spherical or short rod-shaped B2 phase and the softer L1<sub>2</sub> phase form a point-line topological structure similar to spheroiditic pearlitic steels. Load is transmitted through lines (heterogeneous grain boundaries) connected to the hard nodes (B2 and precipitates), achieving mechanical stability and balance through interactions between typical microstructures. This structural design provides an efficient stress transmission path, leading to more uniform stress dispersion, thereby offering better structural strength and stability and prolonging the effect of grain boundary strengthening. As shown in Fig. 13, when the L1<sub>2</sub> phase approaches its load-carrying limit, it transfers partial force to the interfaces connected to it, and these interfaces (uniform precipitated phase and hard B2) then transmit the force to adjacent hard phases, further distributing it to the entire region. Hall-Petch relationship needs to separately consider the strengthening effects caused by the soft and hard phases in the plastic deformation process due to the significant mechanical performance difference between the two phases. Therefore, the Hall-Petch relationship is improved using the concept of mixing rules, as shown in Eq. (32). The values of grain boundary strengthening for EHEA samples are increased to 323 MPa, 284 MPa, and 221 MPa, respectively (Fig. 10). The values of dislocation strengthening for samples A600, A700, and A800 are calculated as 395 MPa, 358 MPa, and 258 MPa, respectively (Fig. 10), using Eq. (24). Due to the dynamic recrystallization caused by warm rolling, the grain boundary and dislocation strengthening effects show a decreasing trend. It can be

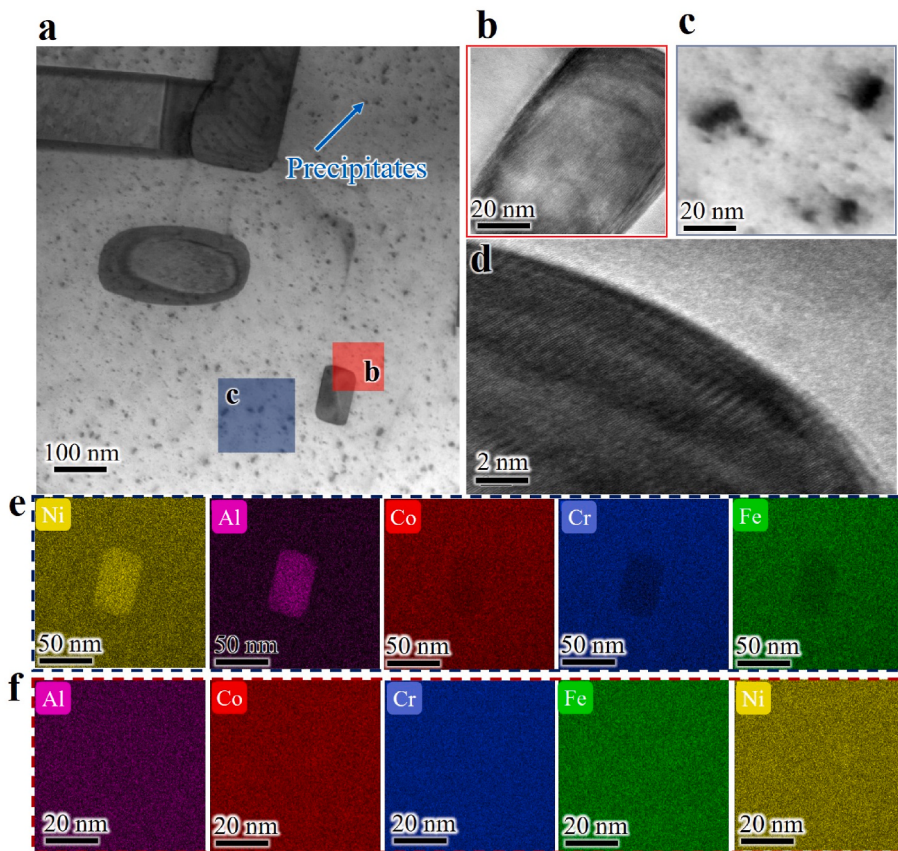


**Fig. 13.** Observation of dispersed nanoscale precipitates and B2 particles in DEA sample by TEM. (a) Distribution of small B2 phase and nanoscale precipitates in L1<sub>2</sub> matrix. (b–c) HRTEM images of the B2 phase and nanoscale precipitates reveal no clear lattice correlation between B2 and the matrix. (e) EDS analysis of the B2 phase. (f) EDS analysis of nanoscale precipitates in (c), showing uniform composition distribution.

observed that the values of grain boundary strengthening and dislocation strengthening in DEA are relatively low among heterogeneous structural metallic materials at the same strength level.

$$\sigma_g = k_1 D_{FCC}^{-\frac{1}{2}} + k_2 D_{BCC}^{-\frac{1}{2}} \quad (32)$$

in the equation,  $k_1$  and  $k_2$  represent the proportionality constants.  $D_{FCC}$  and  $D_{BCC}$  denote the average grain size of the FCC and BCC phases, respectively.

The second-phase particles inside the grains are coherent precipitates with an average diameter smaller than 20 nm (Fig. 13), which impede the migration of dislocations and interfaces surrounding them, following the Orowan-Ashby relationship, contributing to the yield stress with values of 119 MPa, 112 MPa, 120 MPa, respectively. With increasing external load, high-density dislocation accumulation occurs inside the grain, leading to the Orowan strengthening mechanism. The B2 and L1<sub>2</sub> phases, as ultrafine strengthening phases (Fig. 12), are limited in their ability to provide hardening due to the constraint of the dislocation accommodation capacity inside the grains. However, unexpectedly, as shown in Fig. 10, we observed nanoscale B2 structures within the L1<sub>2</sub> grains (Fig. 12(a, b, d, e)), which can also contribute to Orowan strengthening. The complex interaction between the L1<sub>2</sub> matrix and the nano/ultrafine B2 phase further enhances the load-carrying capacity of DEA.

After deformation, the microstructure tends to develop toward equiaxed grains (Fig. 14(a and b)), indicating that the internal stress within the grains is relatively uniform and the possibility of local deformation is reduced. According to Eq. (27), it can be seen that the HDI stress calculated in DEA increases from 33 MPa to 152 MPa, 133 MPa, and 102 MPa, respectively. It is evident that the HDI stress induced

by GNDs pile-up theory is limited, and the piling up of GNDs is not the main factor leading to higher additional strengthening effects in DEA. If all GNDs are arranged on one slip plane, this may result in stress concentrations that are high enough to prematurely promote the nucleation of microcracks. However, the accumulation of GNDs at grain boundaries is necessary to accommodate the non-uniform plastic strain between grains with different orientations (Fig. 14(c)), with which dislocations interact with the grain boundaries. Adjacent grains in the same phase have the same shear modulus, and heterogeneous boundaries cannot endure excessive stress concentration caused by the accumulation of GNDs. Conversely, GNDs will be absorbed by grain boundaries. Once absorbed by heterogeneous boundaries, the theoretical HDI stress value cannot be reached. Phase boundaries typically have higher shear modulus, and B2/L1<sub>2</sub> boundaries can withstand much higher stress concentration than other boundaries. Interestingly, we observe in Fig. 14(f) that GNDs break through the phase interface under stress, activate the GNDs in the hard B2 phase, and further exert the HDI effect. This is different from other single-phase heterogeneous materials, where FCC/BCC boundaries can endure much higher stress concentration than single-phase boundaries, although the density of GNDs is at the same level as that of pile-up, essentially an extension of the same initial array of GNDs. However, the array of GNDs plays a role in activating their slip paths at FCC/BCC heterogeneous boundaries, allowing the same Frank-Read dislocation source to produce multiple GNDs piles, restricting dislocations and plastic strain to the FCC phase, effectively alleviating local stress concentrations in the microstructure, thus triggering significant HDI stress. The current theoretical calculations do not consider the additional strengthening effect caused by the grain boundary strengthening of hard boundaries activated GNDs.

The key to DEA's high yield strength lies in the additional

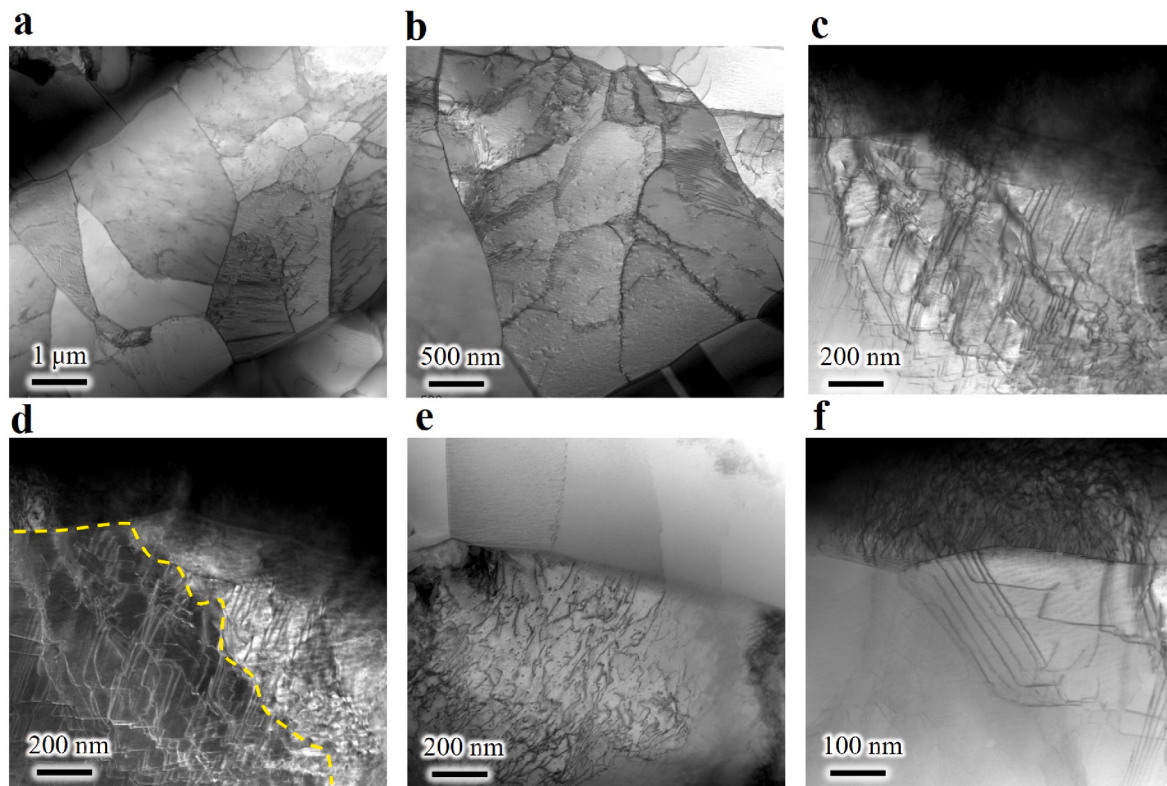


**Fig. 14.** TEM images of fractured A800 sample. (a, b) Typical morphology after fracture. (c, d) Observation of changes in matrix orientation promoting the formation of equiaxed grains under bright-field and dark-field conditions. (e) Abundant dislocations are observed within the L<sub>1</sub><sub>2</sub> phase, while the B<sub>2</sub> phase primarily undergoes grain boundary evolution and grain segmentation. (f) Dislocations breakthrough phase boundary constraints and proliferate, transmitting local grain stresses into another grain, relieving stress concentration in the microstructure, and activating new HDI stress.

strengthening effect brought about by the coupling between dislocations, grain boundaries, and second-phase particles. Linear superposition can calculate the trend of yield strength, but the accuracy still needs improvement. Nonlinear relationships can better predict and quantify the additional coupling effects, and they have excellent generalization ability.

#### 4. Conclusion

In summary, this work is based on the publicly available microstructure parameters and mechanical properties of homogeneous and heterogeneous alloy structures. It proposes a data-driven approach to rapidly extract key physical features related to yield strength and establish a non-linear physical neural network model for predicting the mechanical properties of heterogeneous alloy structures. This model exhibits high predictive accuracy and guides an approximately 2.5-fold increase in the yield strength of ordinary eutectic high-entropy alloys with minimal plastic deformation. By predicting the yield strength and quantitatively calculating the strengthening mechanisms of eutectic high-entropy alloys, the coupling effects between dislocations, grain boundaries, and second-phase particles on yield strength are revealed. Specific conclusions are as follows:

- For the eutectic high-entropy alloy, the average prediction error of yield strength using linear superposition relationships is 13.69%, while the average prediction error using non-linear relationships is 5.49%. Non-linear relationships can directly predict the yield strength of heterogeneous metal materials through key physical quantities, indicating that this research method can be used to describe the relationship between microstructure and macroscopic mechanical properties, providing a theoretical basis for calculating the mechanical properties of structural materials.

- Eutectic high-entropy alloys with multiple strengthening mechanisms were prepared using warm rolling and short-term annealing processes. This method fractures the hard lamellar B<sub>2</sub> phase into fine spherical or short rod-like structures, and even nanoscale B<sub>2</sub> particles can be obtained. The introduction of heterogeneous grain boundaries that do not easily cause stress concentration, coupled with the coupling of dislocations and grain boundaries, extends the strengthening effect of grain boundaries and activates the Hall-Petch effect. Under the influence of temperature, the distribution of nanoscale precipitates becomes more uniform, activating the Orowan strengthening mechanism, relieving stress concentration in the matrix, and forming a more uniform stress organization. This increases the yield strength of EHEA from 384 MPa to 1173 MPa, 1060 MPa, and 837 MPa, the tensile strength from 1046 MPa to 1503 MPa, 1410 MPa, and 1284 MPa, and the elongation from 16% to 12.83%, 14.1%, and 16.5%.

#### CRediT authorship contribution statement

**Jinliang Du:** Methodology, Validation, Formal analysis, Investigation, Data curation, Writing – original draft, Visualization. **Weijie Li:** Validation, Formal analysis, Investigation, Data curation, Visualization. **Zhixin Huang:** Validation, Formal analysis, Investigation, Data curation, Visualization. **Hangqi Feng:** Validation, Formal analysis, Investigation, Data curation, Visualization. **Ying Li:** Conceptualization, Resources, Writing – review & editing, Supervision, Project administration.

#### Declaration of competing interest

The authors declare that they have no known competing financial interests or personal relationships that could have appeared to influence

the work reported in this paper

## Acknowledgments

This work was supported by the National Natural Science Foundation of China (grant numbers 52171290 and 52225108).

## Appendix A. Supplementary data

Supplementary data to this article can be found online at <https://doi.org/10.1016/j.jmrt.2024.03.115>.

## References

- [1] Yin B, Yoshida S, Tsuji N, Curtin WA. Yield strength and misfit volumes of NiCoCr and implications for short-range-order. *Nat Commun* 2020;11:2507. <https://doi.org/10.1038/s41467-020-16083-1>.
- [2] Yan J, Yin S, Asta M, Ritchie RO, Ding J, Yu Q. Anomalous size effect on yield strength enabled by compositional heterogeneity in high-entropy alloy nanoparticles. *Nat Commun* 2022;13:2789. <https://doi.org/10.1038/s41467-022-30524-z>.
- [3] Lee C, Chou Y, Kim G, Gao MC, An K, Brechtl J, et al. Lattice-distortion-enhanced yield strength in a refractory high-entropy alloy. *Adv Mater* 2020;32:2004029. <https://doi.org/10.1002/adma.202004029>.
- [4] Huang LK, Liu F, Huang MX. Accelerating bainite transformation by concurrent pearlite formation in a medium Mn steel: experiments and modelling. *J Mater Sci Technol* 2024;17:211–23. <https://doi.org/10.1016/j.jmst.2023.07.067>.
- [5] Ren J, Zhang Y, Zhao D, Chen Y, Guan S, Liu Y, et al. Strong yet ductile nanolamellar high-entropy alloys by additive manufacturing. *Nature* 2022;608:62–8. <https://doi.org/10.1038/s41586-022-04914-8>.
- [6] Yu Y, Wang Z, Chen B, Zhang S, Du J. Impact of various heat treatment processes and welding speeds on the mechanical properties and microstructures of soft/hard composite joints. *Front Mater* 2024;11:1358912. <https://doi.org/10.3389/fmats.2024.1358912>.
- [7] Zhou Z, Chen M, Li Y. A hybrid analytical method for predicting vibrations in vacuum and water of the sandwich plate with z-direction reinforcements and cavities. *Appl Math Model* 2023;118:71–88. <https://doi.org/10.1016/j.apm.2023.01.024>.
- [8] Moon J, Tabachnikova E, Shumilin S, Hryhorova T, Estrin Y, Brechtl J, et al. Deformation behavior of a Co-Cr-Fe-Ni-Mo medium-entropy alloy at extremely low temperatures. *Mater Today* 2021;50:55–68. <https://doi.org/10.1016/j.mattod.2021.08.001>.
- [9] Li Z, Ma S, Zhao S, Zhang W, Peng F, Li Q, et al. Achieving superb strength in single-phase FCC alloys via maximizing volume misfit. *Mater Today* 2023. <https://doi.org/10.1016/j.mattod.2023.02.012>.
- [10] Manescu TJ, Braun J, Dezelus O. Computational development, synthesis and mechanical properties of face centered cubic Co-free high entropy alloys. *Mater Today Commun* 2022;30:103202. <https://doi.org/10.1016/j.mtcomm.2022.103202>.
- [11] Wang Y, Zeng Q, Wang J, Li Y, Fang D. Inverse design of shell-based mechanical metamaterials with customized loading curves based on machine learning and genetic algorithm. *Comput Methods Appl Mech Eng* 2022;401:115571. <https://doi.org/10.1016/j.cma.2022.115571>.
- [12] Liu H, Wei J, Dong J, Zhou Y, Chen Y, Wu Y, et al. The synergy between cementite spheroidization and Cu alloying on the corrosion resistance of ferrite-pearlite steel in acidic chloride solution. *J Mater Sci Technol* 2021;84:65–75. <https://doi.org/10.1016/j.jmst.2020.12.031>.
- [13] Bata V, Pereloma EV. An alternative physical explanation of the Hall-Petch relation. *Acta Mater* 2004;52:657–65. <https://doi.org/10.1016/j.actamat.2003.10.002>.
- [14] Weertman JR. Hall-Petch strengthening in nanocrystalline metals. *Mater Sci Eng A* 1993;166:161–7. [https://doi.org/10.1016/0921-5093\(93\)90319-A](https://doi.org/10.1016/0921-5093(93)90319-A).
- [15] Fan Z, Gao F, Wang Y, Men H, Zhou L. Effect of solutes on grain refinement. *Festschr Honor Brian Cantor* 2022;123:100809. <https://doi.org/10.1016/j.pmatcs.2021.100809>.
- [16] He X, Dong H-W, Ren Z, Zhao S-D, Wang K, Hu Y, et al. Inverse-designed single-phase elastic metasurfaces for underwater acoustic vortex beams. *J Mech Phys Solid* 2023;174:105247. <https://doi.org/10.1016/j.jmps.2023.105247>.
- [17] Jia C, Zheng C, Li D. Cellular automaton modeling of austenite formation from ferrite plus pearlite microstructures during intercritical annealing of a C-Mn steel. *J Mater Sci Technol* 2020;47:1–9. <https://doi.org/10.1016/j.jmst.2020.02.002>.
- [18] He BB, Hu B, Yen HW, Cheng GJ, Wang ZK, Luo HW, et al. High dislocation density-induced large ductility in deformed and partitioned steels. *Science* 2017;357:1029–32. <https://doi.org/10.1126/science.aan0177>.
- [19] Wang M, He BB, Huang MX. Strong and ductile Mg alloys developed by dislocation engineering. *J Mater Sci Technol* 2019;35:394–5. <https://doi.org/10.1016/j.jmst.2018.09.033>.
- [20] Moon J, Bouaziz O, Kim HS, Estrin Y. Twinning engineering of a CoCrFeMnNi high-entropy alloy. *Scr Mater* 2021;197:113808. <https://doi.org/10.1016/j.scriptamat.2021.113808>.
- [21] Qiao K, Wang K, Wang J, Hao Z, Xiang Y, Han P, et al. Microstructural evolution and deformation behavior of friction stir welded twin-induced plasticity steel. *J Mater Sci Technol* 2024;16:68–81. <https://doi.org/10.1016/j.jmst.2023.05.053>.
- [22] Chen H, Hu L, Ju M, Xie K, Gao A, Zheng C, et al. Chiral smart bionic skin film with changeable structural colors and tunable luminescence by polymer-assisted supramolecular assembly of the photonic crystals. *Appl Mater Today* 2022;29:101654. <https://doi.org/10.1016/j.apmt.2022.101654>.
- [23] Wu YC, Kuo CN, Wu TH, Liu TY, Chen YW, Guo XH, et al. Empirical rule for predicting mechanical properties of Ti-6Al-4V bone implants with radial-gradient porosity bionic structures. *Mater Today Commun* 2021;27:102346. <https://doi.org/10.1016/j.mtcomm.2021.102346>.
- [24] Sun J, Wang H, Xu B, Jiang L, Guo S, Sun X, et al. Making low-alloyed steel strong and tough by designing a dual-phase layered structure. *Acta Mater* 2022;227:117701. <https://doi.org/10.1016/j.actamat.2022.117701>.
- [25] Guo M, Jiang J, Shen Z, Lin Y, Nan C-W, Shen Y. High-energy-density ferroelectric polymer nanocomposites for capacitive energy storage: enhanced breakdown strength and improved discharge efficiency. *Mater Today* 2019;29:49–67. <https://doi.org/10.1016/j.jmattod.2019.04.015>.
- [26] Liu P, Hou B, Wang A, Xie J, Wang Z, Ye F. Superior strength-plasticity synergy in a heterogeneous lamellar Ti2AlC/TiAl composite with unique interfacial microstructure. *J Mater Sci Technol* 2023;159:21–32. <https://doi.org/10.1016/j.jmst.2023.03.011>.
- [27] Wang P, Bu Y, Liu J, Li Q, Wang H, Yang W. Atomic deformation mechanism and interface toughening in metastable high entropy alloy. *Mater Today* 2020;37:64–73. <https://doi.org/10.1016/j.mattod.2020.02.017>.
- [28] Gao Q, Zhang X, Feng S, Han Z, Chen C, Wang T, et al. Achieving ultra-high mechanical properties in metastable Co-free medium entropy alloy via hierarchically heterogeneous microstructure. *J Mater Sci Technol* 2024;183:175–83. <https://doi.org/10.1016/j.jmst.2023.10.022>.
- [29] Sun LG, Wu G, Wang Q, Lu J. Nanostructural metallic materials: structures and mechanical properties. *Mater Today* 2020;38:114–35. <https://doi.org/10.1016/j.mattod.2020.04.005>.
- [30] Zhu L, Ruan H, Sun L, Guo X, Lu J. Constitutive modeling of size-dependent deformation behavior in nano-dual-phase glass-crystal alloys. *Int J Plast* 2021;137:102918. <https://doi.org/10.1016/j.ijplas.2020.102918>.
- [31] Kang HB, Poudel B, Li W, Lee H, Saparamadu U, Nozariasbmarz A, et al. Decoupled phonon-electron transport in multi-phase n-type half-Heusler nanocomposites enabling efficient high temperature power generation. *Mater Today* 2020;36:63–72. <https://doi.org/10.1016/j.mattod.2020.01.002>.
- [32] Sathyamoorthy P, Kim HS. High-entropy alloys with heterogeneous microstructure: processing and mechanical properties. *Festschr Honor Brian Cantor* 2022;123:100709. <https://doi.org/10.1016/j.pamatsci.2020.100709>.
- [33] Du J, Li J, Feng Y, Ning J, Liu S, Zhang F. Effect of layered heterogeneous microstructure design on the mechanical behavior of medium carbon steel. *Mater Des* 2022;221:110953. <https://doi.org/10.1016/j.matedes.2022.110953>.
- [34] Du JL, Feng YL, Zhang M. Construction of a machine-learning-based prediction model for mechanical properties of ultra-fine-grained Fe-C alloy. *J Mater Res Technol* 2021;15:4914. <https://doi.org/10.1016/j.jmrt.2021.10.111>.
- [35] Sun LG, Wu G, Wang Q, Lu J. Nanostructural metallic materials: structures and mechanical properties. *Mater Today* 2020;38:114–35. <https://doi.org/10.1016/j.mattod.2020.04.005>.
- [36] Chen Y, Fang Y, Fu X, Lu Y, Chen S, Bei H, et al. Origin of strong solid solution strengthening in the CrCoNi-W medium entropy alloy. *J Mater Sci Technol* 2021;73:101–7. <https://doi.org/10.1016/j.jmst.2020.08.058>.
- [37] Zhang L, Dong H, Li P, Wu B, Ma Y, Huang L, et al. Multiscale microstructural consideration of enhanced shear strength in TiAl intermetallic/K4169 alloy composite joints prepared by vacuum brazing with (Ti, Zr)-Ni-based amorphous filler metal. *J Mater Sci Technol* 2024;172:51–70. <https://doi.org/10.1016/j.jmst.2023.06.058>.
- [38] Ji W, Wu MS. Inhibiting the inverse Hall-Petch behavior in CoCuFeNiPd high-entropy alloys with short-range ordering and grain boundary segregation. *Scr Mater* 2022;221:114950. <https://doi.org/10.1016/j.scriptamat.2022.114950>.
- [39] Jung H, Lee J, Gu GH, Lee H, Seo S-M, Zargaran A, et al. Multiscale defects enable synergistic improvement in yield strength of CrCoNi-based medium-entropy alloy fabricated via laser-powder bed fusion. *Addit Manuf* 2023;61:103360. <https://doi.org/10.1016/j.addma.2022.103360>.
- [40] Liebig JP, Krauß S, Göken M, Merle B. Influence of stacking fault energy and dislocation character on slip transfer at coherent twin boundaries studied by micropillar compression. *Acta Mater* 2018;154:261–72. <https://doi.org/10.1016/j.actamat.2018.05.037>.
- [41] Woo W, Kim YS, Chae HB, Lee SY, Jeong JS, Lee CM, et al. Competitive strengthening between dislocation slip and twinning in cast-wrought and additively manufactured CrCoNi medium entropy alloys. *Acta Mater* 2023;246:118699. <https://doi.org/10.1016/j.actamat.2023.118699>.
- [42] Naik SN, Walley SM. The Hall-Petch and inverse Hall-Petch relations and the hardness of nanocrystalline metals. *J Mater Sci* 2020;55:2661–81. <https://doi.org/10.1007/s10853-019-04160-w>.
- [43] Ren CX, Wang Q, Zhang ZJ, Zhang P, Zhang ZF. Surface strengthening behaviors of four structural steels processed by surface spinning strengthening. *Mater Sci Eng A* 2017;704:262–73. <https://doi.org/10.1016/j.msea.2017.08.007>.
- [44] Li Q-J, Sheng H, Ma E. Strengthening in multi-principal element alloys with local-chemical-order roughened dislocation pathways. *Nat Commun* 2019;10:3563. <https://doi.org/10.1038/s41467-019-11464-7>.
- [45] Dong Z, Ma Z, Yu L, Liu Y. Achieving high strength and ductility in ODS-W alloy by employing oxide@W core-shell nanopowder as precursor. *Nat Commun* 2021;12:5052. <https://doi.org/10.1038/s41467-021-25283-2>.

- [46] Basu I, Ocelfk V, De Hosson JThM. BCC-FCC interfacial effects on plasticity and strengthening mechanisms in high entropy alloys. *Acta Mater* 2018;157:83–95. <https://doi.org/10.1016/j.actamat.2018.07.031>.
- [47] Shen Y-N, Chang Y-T, Chen C-H. Alloying-assisted precipitation strengthening of Ti50Ni15Pd25Cu10 shape memory alloy. *Mater Sci Eng A* 2021;821:141636. <https://doi.org/10.1016/j.msea.2021.141636>.
- [48] Li AX, Liu XS, Li R, Yu SB, Jiang MH, Zhang JS, et al. Double heterogeneous structures induced excellent strength–ductility synergy in Ni40Co30Cr20Al5Ti5 medium-entropy alloy. *J Mater Sci Technol* 2024;181:176–88. <https://doi.org/10.1016/j.jmst.2023.10.011>.
- [49] Rao Z, Tung P-Y, Xie R, Wei Y, Zhang H, Ferrari A, et al. Machine learning–enabled high-entropy alloy discovery. *Science* 2022;378:78–85. <https://doi.org/10.1126/science.abo4940>.
- [50] Juan Y, Dai Y, Yang Y, Zhang J. Accelerating materials discovery using machine learning. *J Mater Sci Technol* 2021;79:178–90. <https://doi.org/10.1016/j.jmst.2020.12.010>.
- [51] Zhang J, Cai C, Kim G, Wang Y, Chen W. Composition design of high-entropy alloys with deep sets learning. *npj Comput Mater* 2022;8:89. <https://doi.org/10.1038/s41524-022-00779-7>.
- [52] Wright LG, Onodera T, Stein MM, Wang T, Schachter DT, Hu Z, et al. Deep physical neural networks trained with backpropagation. *Nature* 2022;601:549–55. <https://doi.org/10.1038/s41586-021-04223-6>.
- [53] Benesty J, Chen J, Huang Y, Cohen I. Pearson correlation coefficient. In: Cohen I, Huang Y, Chen J, Benesty J, editors. *Noise reduct*. Speech process. Berlin, Heidelberg: Springer Berlin Heidelberg; 2009. p. 1–4. [https://doi.org/10.1007/978-3-642-00296-0\\_5](https://doi.org/10.1007/978-3-642-00296-0_5).
- [54] Darst BF, Malecki KC, Engelman CD. Using recursive feature elimination in random forest to account for correlated variables in high dimensional data. *BMC Genet* 2018;19:65. <https://doi.org/10.1186/s12863-018-0633-8>.
- [55] Cheng Z, Wan T, Bu L, Lu L. Effect of volume fractions of gradient transition layer on mechanical behaviors of nanotwinned Cu. *Acta Mater* 2023;242:118456. <https://doi.org/10.1016/j.actamat.2022.118456>.
- [56] Chen L, Cao T, Wei R, Tang K, Xin C, Jiang F, et al. Gradient structure design to strengthen carbon interstitial Fe40Mn40Co10Cr10 high entropy alloys. *Mater Sci Eng A* 2020;772:138661. <https://doi.org/10.1016/j.msea.2019.138661>.
- [57] Hecht-Nielsen R. Counterpropagation networks. *Appl Opt* 1987;26:4979–84. <https://doi.org/10.1364/AO.26.004979>.
- [58] Ferguson JB, Schultz BF, Venugopalan D, Lopez HF, Rohatgi PK, Cho K, et al. On the superposition of strengthening mechanisms in dispersion strengthened alloys and metal–matrix nanocomposites: considerations of stress and energy. *Met Mater Int* 2014;20:375–88. <https://doi.org/10.1007/s12540-014-2017-6>.
- [59] Li Q, Li G, Lin X, Zhu D, Jiang J, Shi S, et al. Development of a high strength Zr/Sc/Hf-modified Al-Mn-Mg alloy using Laser Powder Bed Fusion: design of a heterogeneous microstructure incorporating synergistic multiple strengthening mechanisms. *Addit Manuf* 2022;57:102967. <https://doi.org/10.1016/j.addma.2022.102967>.
- [60] Wan T, Cheng Z, Bu L, Lu L. Work hardening discrepancy designing to strengthening gradient nanotwinned Cu. *Scr Mater* 2021;201:113975. <https://doi.org/10.1016/j.scriptamat.2021.113975>.
- [61] Du J, Liu G, Feng Y, Feng H, Li T, Zhang F. Strength and ductility enhancement of plain carbon steel by heterostructure design. *Mater Sci Eng A* 2023;868:144770. <https://doi.org/10.1016/j.msea.2023.144770>.
- [62] Shi P, Li R, Li Y, Wen Y, Zhong Y, Ren W, et al. Hierarchical crack buffering triples ductility in eutectic herringbone high-entropy alloys. *Science* 2021;373:912–8. <https://doi.org/10.1126/science.abf6986>.
- [63] Wani IS, Bhattacharjee T, Sheikh S, Bhattacharjee PP, Guo S, Tsuji N. Tailoring nanostructures and mechanical properties of AlCoCrFeNi2.1 eutectic high entropy alloy using thermo-mechanical processing. *Mater Sci Eng A* 2016;675:99–109. <https://doi.org/10.1016/j.msea.2016.08.048>.
- [64] Tan C, Weng F, Sui S, Chew Y, Bi G. Progress and perspectives in laser additive manufacturing of key aeroengine materials. *Int J Mach Tools Manuf* 2021;170:103804. <https://doi.org/10.1016/j.ijmachtools.2021.103804>.
- [65] Dollar M, Bernstein IM, Thompson AW. Influence of deformation substructure on flow and fracture of fully pearlitic steel. *Acta Metall* 1988;36:311–20. [https://doi.org/10.1016/0001-6160\(88\)90008-9](https://doi.org/10.1016/0001-6160(88)90008-9).
- [66] Ren J, Zhang Y, Zhao D, Chen Y, Guan S, Liu Y, et al. Strong yet ductile nanolamellar high-entropy alloys by additive manufacturing. *Nature* 2022;608:62–8. <https://doi.org/10.1038/s41586-022-04914-8>.
- [67] Wu Q, He F, Li J, Kim HS, Wang Z, Wang J. Phase-selective recrystallization makes eutectic high-entropy alloys ultra-ductile. *Nat Commun* 2022;13:4697. <https://doi.org/10.1038/s41467-022-32444-4>.
- [68] Du J, Li J, Feng Y, Li Y, Zhang F. Exploring nonlinear strengthening in polycrystalline metallic materials by machine learning methods and heterostructure design. *Int J Plast* 2023;164:103587. <https://doi.org/10.1016/j.ijplas.2023.103587>.
- [69] Du J, Feng Y, Liu G, Liao X, Zhang F. Strong yet ductile bionic steel by mitigating local stress concentration function. *J Mater Sci Technol* 2024. <https://doi.org/10.1016/j.jmst.2023.12.066>.
- [70] Gao X, Lu Y, Zhang B, Liang N, Wu G, Sha G, et al. Microstructural origins of high strength and high ductility in an AlCoCrFeNi2.1 eutectic high-entropy alloy. *Acta Mater* 2017;141:59–66. <https://doi.org/10.1016/j.actamat.2017.07.041>.